

1 Phased Array Analysis Incorporating the Continuous Wavelet Transform

2
3 Charles A. Langston
4 clangstn@memphis.edu

5
6
7
8
9
10
11
12 Center for Earthquake Research and Information
13 University of Memphis

14
15
16
17
18
19
20
21
22
23
24
25 To be submitted
26 Bulletin of the Seismological Society of America

27
28
29
30
31
32 December 4, 2020
33
34
35
36
37
38

Abstract

Non-linear block thresholding of the continuous wavelet transform (CWT) of 2D phased array signals offer high time-resolution solutions for analyzing seismograms of local and regional seismic events. An initial denoising step on an array ensemble reveals those regions of the scale-time plane that contain high signal-to-noise arrivals. Individual seismic phase arrivals in ensemble, denoised seismograms can be partitioned using scale-time gating where CWT wave packets of an individual seismic phase on the scale-time plane for a reference array element are time-correlated with all other elements to find an optimum time shift for the phase across all elements. The seismic phase is then clipped out of the CWT of each array element using this optimal time shift for further analysis. The seismogram can be separated into component seismic waves for a detailed view of wave characteristics such as slowness and arrival azimuth using conventional frequency-wavenumber methods. However, the process can be taken further by using the CWT of each phase to construct high time-resolution signal beams over CWT scale. Local explosion data from the 2016 IRIS Wavefields community experiment in northern Oklahoma are used to demonstrate these techniques in separating surface wave modes and body waves and examining the scattering of regional phases. High resolution CWT processing in the 1 to 3 Hz band for northern Oklahoma reveals horizontal Rayleigh wave refraction and multipathing. Rayleigh wave phase velocity dispersion measurements are used to construct a 1D velocity model under the IRIS experiment. Scale-time gating helps expose near-source surface reflections from a local M3.6 earthquake that are used to verify the 4km source depth obtained from a published regional moment tensor solution.

Introduction

The analysis of seismic signals using phased arrays of seismometers is the basis of much of nuclear verification seismology where detection, location, and discrimination of earthquakes from explosions are primary goals (Filson, 1975; Douglas, 2002; Rost and Thomas, 2002; Havskov and Alguacil, 2004). Numerous methods and array designs have been developed primarily for analyzing the principal wave attributes of frequency, horizontal phase velocity, and signal back azimuth for both source and structure studies (Capon et al., 1967; Haubrich, 1968; Capon, 1969; 1970; Claasen, 1985; Mykkeltveit et al., 1983; Mykkeltveit, 1985; Nawab et al., 1985; Abrahamson et al., 1987; Goldstein and Archuleta, 1987; Kvaerna, 1989; Gupta et al., 1990; Kvaerna and Ringdahl, 1992; Wagner and Owens, 1993; Kushnir, 1996; Lindfors, 1996; Stump et al., 2004; Harris and Kvaerna, 2010; Gibbons et al., 2011; Gibbons, 2014). An important attribute of phased array beam forming is the ability of the array to improve the signal-to-noise ratio (SNR) of incident signals by shifting, then stacking in the time or frequency domains at the appropriate azimuth and vector slowness of the incident wave. The improvement in SNR is often estimated by assuming a normally distributed background noise field so that noise is reduced by \sqrt{N} , where N is the number of sensors in the array (Capon et al., 1967; Aki and Richards, 1980). Improving the SNR improves the chances of event detection. However, wave coherence is a major issue in phased array signal processing and is a function of the wave scattering properties of Earth structure local to the array (e.g., Toksöz et al., 1991; Al-Shukri et al., 1995). Although there are many ideal array designs that can theoretically focus individual seismic phases, array performance is always degraded by noise and waveform decorrelation. Array design is almost always an issue as well, since field conditions may preclude optimum

geometries or numbers of deployed sensors degrading the signal beam through creation of side lobes in wavenumber space making it difficult to separate interfering seismic phases.

In this paper I extend the concepts introduced in Langston and Mousavi (2019), referred to as “L&M” in the remaining part of this paper, for using the continuous wavelet transform (CWT) to remove noise and partition waveforms into individual seismic phases to improve beam forming with a phased array. The initial step of denoising an array dataset using non-linear thresholding can improve the SNR by an order of magnitude or more before any array analysis is attempted. “Scale-time gating” will be introduced to separate target seismic phases over the array in the wavelet domain for individual frequency-wavenumber analysis. I then suggest an additional step of beam forming within the CWT domain that produces array beams at the sampling rate of the original time series. A relatively simple measure of beam coherence is also used to ascertain what parts of the seismic wavefield are coherent across the array and which aren’t to serve as an indication of the quality of the phase interpretation.

These methods will be demonstrated using local explosion data recorded by the 2016 IRIS Wavefields experiment in northern Oklahoma (Sweet et al., 2018). The array analysis will make it possible to investigate high frequency Rayleigh wave multipathing and the composition of body waves that propagate in the local waveguide of Paleozoic sediments. Although I apply the methods to local wave propagation and a high frequency seismic array, they can be used for any phased array. In addition, the separation of seismic phases with scale-time gating significantly improves seismic gradiometry using geodetic seismic arrays since the phase separation step can remove artifacts caused by phase interference (Langston, 2007; Langston and Liang, 2008).

Data

The 2016 IRIS Wavefields seismic experiment was designed by an interested community group to collect densely sampled array data in an area of active induced seismicity in northern Oklahoma (Sweet et al., 2018) (Figure 1). 247 three-component, 5 Hz Fairfield Nodal Zland nodal seismometers were deployed in two NS 5 km lines and one EW 13 km line. 112 of these seismometers were deployed in a 800x800m, 7 level, nested gradiometer configuration. 18 broadband seismometers were deployed as a “Golay 3x6” regional array with an approximate aperture of 6km. 9 infrasound instruments were sited with 9 of the broadbands to help in discriminating acoustic signals that might be recorded seismically. Data from the experiment are stored at the IRIS Data Management Center under the network code YW for 2016.

The nodal seismometers were deployed over the time interval of 22 June to 27 July and passively recorded hundreds of local earthquakes, teleseisms, and other regional events. The broad band Golay array was kept in place until late November to catch aftershocks from the M5.8 Pawnee earthquake that occurred in September just before the originally planned decommissioning of the experiment.

On 14 July and 16 July 2016 the Air Force Technical Applications Command (AFTAC) commissioned an explosion seismic experiment performed by the IRIS Source Facility at the University of Texas, El Paso (Cleat Zeiler, personal communication 2017). The experiment consisted of 4 borehole explosions of varying sizes set and detonated at 3 different azimuths and distances from the array. In this paper, I use the data from the 2000 lb explosion detonated approximately 35 km to the northwest which is the same event as used in L&M (Figure 1).

A cross-shaped array was subset from the YW array from the stations located at the eastern crossing of the EW and NS arms of the linear deployments. This subarray has an aperture of 3

km and densely samples wave lengths of 3 to 3.5 km as demonstrated by its co-array diagram (Figure 2). This array was chosen to investigate the wave characteristics of the high frequency explosion waveforms in the band of 1 to 10 Hz.

The raw waveform data were recorded at 200 sps. The only initial processing applied to the data was to remove the nominal instrument response of the 5 Hz nodal instruments and applying a trapezoidal zero-phase filter in the band 0.05 to 80 Hz with corner frequencies of 0.5 and 50 Hz.

CWT Array Analysis

CWT Denoising

L&M outline a method for using the CWT to efficiently remove noise from individual seismic traces and to partition a waveform into component seismic phases. These processes will be quickly summarized before presenting their applications to phased array processing.

The Morlet-Grossmann definition (Grossmann et al., 1989; Starck et al., 2010) for the CWT is

$$W(a, \tau) = \frac{1}{\sqrt{a}} \int_{-\infty}^{+\infty} f(t) \psi^* \left(\frac{t - \tau}{a} \right) dt \quad (1)$$

where the * represents the complex conjugate of the function. The CWT is simply a correlation of the signal, $f(t)$, with a scaled basis function $\psi(t)$. In general, the basis function is complex and is termed the “mother wavelet”. The wavelet coefficient, $W(a, \tau)$ is also complex and can be represented in the Fourier domain as

$$\hat{W}(a, \omega) = \sqrt{a} \hat{f}(\omega) \hat{\psi}^*(a\omega) . \quad (2)$$

The CWT is a linear operation and has an exact inverse transform given by the double integral

$$f(t) = \frac{1}{C} \int_0^\infty \int_{-\infty}^{+\infty} \frac{1}{\sqrt{a}} W(a, \tau) \psi\left(\frac{t-\tau}{a}\right) \frac{da d\tau}{a^2} \quad (3)$$

where C is found from a Parseval-like integral

$$C = \int_0^{+\infty} \frac{\hat{\psi}^*(\omega) \hat{\psi}(\omega)}{\omega} d\omega \quad (4)$$

that requires the basis function to have zero mean for this integral to be bounded at $\omega = 0$.

I continue to use Morlet's wavelet as the mother wavelet in all computations in this paper.

The first step in the phased array analysis is to remove the obvious noise contained in the seismograms of all array elements. This is done using a soft thresholding process where the wavelet coefficients less than a predetermined noise threshold are removed entirely and those above the threshold reduced by the noise estimate. This is given by

$$\tilde{W}(a, \tau) = \begin{cases} \text{sign}[W(a, \tau)](|W(a, \tau)| - \beta(a)) & \text{if } |W(a, \tau)| \geq \beta(a) \\ 0 & \text{otherwise} \end{cases} \quad (5)$$

where

$$\text{sign}[W(a, \tau)] = \frac{W(a, \tau)}{|W(a, \tau)|} \quad (6)$$

The threshold level, $\beta(a)$, is determined by examining the statistics of the wavelet coefficients for a noise time window before or after the signal and constructing its empirical cumulative distribution function (ECDF_a) where

$$\beta(a) = \text{ECDF}_a^{-1}(P = 0.99) \quad (7)$$

at the 99% confidence level.

This process was applied to the explosion data recorded by the cross array. In addition, as mentioned in L&M, a scale band reject filter was applied to the remaining coefficients on the

scale-time plane for scales greater than 1s to remove long period, high scale, artifacts that remained from the soft threshold step. This improved the SNR from less than 1 as seen visually in the instrument-corrected data to approximately 200 for the soft-thresholded waveforms, taking the maximum amplitudes of the pre-event noise as the noise measure and the maximum of the resulting signal as the signal measure. These pre-processing steps primarily find those regions of the scale-time plane that have high SNR. As we will see in the array processing, waveforms for the cross array are highly correlated creating close to theoretical beam patterns in the analysis showing that seismic phases are not significantly distorted in the denoising process. However, as pointed out in L&M, if the SNR is low even in the primary signal area of the scale-time plane, significant signal loss and distortion can occur.

Signal Decomposition and Scale-Time Gating

At this point the denoised waveforms can be processed using standard array beamforming techniques. However, the waveforms of the AFTAC explosion show many interesting and discrete seismic phases which appear to clearly separate on the scale-time plane (Figure 3). L&M show that it is straightforward to pick these phases on the scale-time plane by choosing an enclosing polygon and then using the inverse CWT to obtain their time domain waveform. This process can be tedious if manually applied to all 81 stations of the cross array.

The strategy for gating particular phases from individual elements of an array is to choose a reference station near the center of the array, delimit the phase of interest by encompassing it with a polygon on the CWT scalogram and then using this block of the CWT in a two-dimensional correlation with the scalograms of all other elements of the array. Figure 3 shows the result of using the vertical component of station 3016 to pick the fundamental mode surface

197 wave and then finding the maximum of the correlation of the modulus of the CWT coefficient in
198 this block with those for station 3001, the station located nearest the source.

199 In the process of examining the time shifts obtained from the scale-time gating procedure, it
200 was found that the time shifts were sometimes inconsistent with the expected move-out of the
201 seismic phase, if the modulus of wavelet coefficients was used directly. Indeed, even performing
202 the 2D correlation on the same signal that the block of interest was taken from did not always
203 yield a zero time lag; adjacent wavelet coefficients outside of the block could contaminate the
204 correlation. Although the inferred time shifts were very small compared to the duration of the
205 windowed signal, it appeared that non-unique correlations of the wavelet coefficient modulus
206 could cause problems with the method. Through numerical experimentation, I found that using a
207 power of $|W|^n$ before correlation was much more effective in giving appropriate time shifts.
208 Using $n=3$ gave results in line with the observed moveout of the seismic phases. Using a power
209 of the wavelet coefficients weights the correlation towards the highest amplitude coefficients in
210 the block which, presumably, are less affected by noise.

211 Scale-time gating was effective in delimiting the fundamental mode Rayleigh wave (Figure
212 4) and first higher mode Rayleigh wave (not shown) from all array elements. Detailed results
213 from the dispersion analysis will be discussed later.

214 Scale-time gating was found to work well with the surface wave modes but was
215 problematical with an attempt at gating the P wave trains from the explosion. A straightforward
216 choice of the P wave CWT block (Figure 5a) gave poor results (Figure 6a) since the correlation
217 process often chose the first higher mode over the P wave train. This problem was solved by
218 choosing a block defined by both the fundamental and first higher modes to get the optimum

mode time shifts and then zeroing out the CWT coefficients within the mode block (Figure 5b).
The remainder gives the desired P wave train (Figure 6b).

Broad Band/Narrow Band Frequency-Wavenumber Analysis

The scale-time gated data for the various crustal phases can now be analyzed using standard techniques after the inverse CWT. As an example, I show a detailed dispersion analysis of the fundamental mode Rayleigh wave using a common broad band/narrow band method (Nawab et al., 1985). Figure 4b shows the Rayleigh wave slowness response over the entire frequency band of 1 to 3 Hz encompassing the fundamental mode data. The peak of the response is clearly about 15° north of the expected great circle wave path showing the effects of possible horizontal refraction and multipathing in these high frequency local surface waves.

Narrow band frequency-wavenumber spectra were taken for bandwidths of 0.125 Hz (Figures 4 and 7) and show smooth changes in phase velocity and back azimuth across the array with frequency over the band of 1 to 2.5 Hz, probably due to horizontal refraction due to velocity heterogeneity in the upper kilometer of the crust. At frequencies higher than 2.5 Hz, the slowness spectra break up into multiple peaks showing several surface wave arrivals with different slowness and azimuths.

Error bounds on slowness and back azimuth were estimated by an algorithm that uses the theoretical array response over the frequency band to estimate the variation within the 90% amplitude level. The theoretical response is shifted to the observed maximum peak, scaled by the observed peak amplitude and then subtracted from the data f-k spectrum. The peak of the remaining part of the spectrum is then taken as the signature of the next observed wave and the process repeated to estimate its errors. This process was done to find all peaks in the original slowness spectra down to a level of 0.3 of the maximum peak. As Figure 7 shows, the peaks of

the theoretical narrow band slowness spectra have similar widths as the peaks seen in the data, so using the theoretical spectra for the error estimate is reasonable.

Likewise, broadband slowness spectra of P1 and P2 phases over the frequency band of 5 to 15 Hz show quite focused estimates for these P arrivals (Figure 8). Back azimuths are within a degree of the theoretical great circle path to the event showing little evidence for horizontal refraction due to velocity heterogeneity.

Beam Forming in the Scale-Time Domain

Up to this point, I have utilized the CWT to remove noise from the original seismograms, separate various phases in the seismogram, and then designed a scale-time gating method to analyze particular arrivals of interest using a phased array. The resulting seismograms were then analyzed using standard Fourier array beam forming such as narrow-band or broad-band methods. Narrow-band analysis is a natural method for determining surface wave dispersion since phase velocity spectral methods are tied directly to solutions for surface wave propagation in vertically inhomogeneous media. However, the question arises: can the wavelet coefficients themselves be used to estimate wave slowness and azimuth? If so, what are advantages to this kind of phased array analysis?

Using equation (1), the CWT of the k th array channel, $f_k(t)$, is given by

$$W_k(a, \tau) = \frac{1}{\sqrt{a}} \int_{-\infty}^{+\infty} f_k(t) \psi^* \left(\frac{t - \tau}{a} \right) dt . \quad (8)$$

The wavelet coefficients, W_k , are the time series that make up the scalogram, or scale-time plot of the transformed time series data. Particular seismic phases have specific locations on the scale-time plane defined by time lags due to their wave propagation characteristics and

264 frequency content of the medium's Green's function and source excitation. Any time shifts
 265 undergone by waves in $f_k(t)$ will show up in the wavelet coefficients. This can be easily shown
 266 by assuming a shifted signal $f_k(t-b)$, where b is a constant:

$$267 \quad I = \frac{1}{\sqrt{a}} \int_{-\infty}^{+\infty} f(t-b) \psi^* \left(\frac{t-\tau}{a} \right) dt . \quad (9)$$

268 Let $T=t-b$ so that $t=T+b$, and $dT=dt$. This gives

$$269 \quad I = \frac{1}{\sqrt{a}} \int_{-\infty}^{+\infty} f_k(T) \psi^* \left(\frac{T-(\tau-b)}{a} \right) dT . \quad (10)$$

$$= W(a, \tau - b)$$

270 Therefore, beams of each wavelet scale time series can be made by shifting each scale by an
 271 assumed plane wave time shift across an array and stacking the shifted scalograms for each array
 272 element. A narrow-scale band beam can be defined by

$$273 \quad W_{Beam}(a, \tau) = \sum_k W_k(a, \tau + p_x x_k + p_y y_k) \quad (11)$$

274 by summing the lagged wavelet series for a particular scale over all array elements after
 275 correcting for plane wave moveout across the array for an assumed slowness vector (p_x, p_y) . In
 276 analogy to a broad-band stack, wavelet time series for a specified scale band can be summed:

$$277 \quad \bar{W}_{Beam}(\tau) = \sum_j \sum_k W_k(a_j, \tau + p_x x_k + p_y y_k) . \quad (12)$$

278 In practice, these sums are made by discretizing the slowness plane, making the plane wave
 279 time lag corrections to the scalogram and summing. Constructive interference between the array
 280 elements will give power maxima on the slowness plane where power is defined as the square of
 281 the beam moduli.

282 These array beams are continuous time series so they can give a continuous estimate of
 283 slowness as a function of time. An additional stacking process can be made by integrating the

beam power over a time window to get the cumulative energy of discrete signals. An implication of these processes is that each sampled spot on the slowness plane will be a time series so that a very large three-dimensional array of slowness spectra data is generated.

Figure 9 displays an example of a broad scale band beam forming according to equation (12). A scale bandpass of 0.1 to 0.5 s has been used to block filter the data. By “block filtering”, I mean that all wavelet coefficients between 0.1 and 0.5 s have been used in the beam form and that all other coefficients have been set to zero. Figure 9 shows the resulting broadband scale-slowness beam for 5 different time points. In addition, the quality of the beam form is assessed by using a simple statistic based on the power of the peak, P_{max} compared to the integrated power over the entire slowness plane, P_{Total} :

$$R = \frac{P_{max}}{P_{Total}} . \quad (13)$$

In Figure 9, a phase velocity and back azimuth for a particular time is colored red when $R \geq 0.5$ or blue when $R < 0.5$. High values of R represent broadband scale slowness images that have single prominent peaks, such as for P1 and S in Figure 9, while low values describe diffuse beams or multiple peaks.

Note that this beamforming analysis can be used to identify arrivals in the seismogram that are relatively coherent across the array as well as arrivals that do not produce good beams. Recall that this waveform was the result of removing the higher and fundamental Rayleigh modes from the denoised seismograms to expose the lower scale parts that seemed to be dominated by P wave arrivals. The CWT beam forming has uncovered what is likely the direct S wave from the explosion traveling at a horizontal phase velocity of about 3.5 km/s. The P1 phase appears to be a head wave with a velocity of about 6.4 km/s followed by a slower velocity P2 phase that may be the start of P reverberations in the near-surface Paleozoic sediments. The

P2 wave train gradually gets slower with time attaining horizontal velocities of about 4 km/s until the S wave arrives. Coda waves show scatter in slowness and back azimuth indicating multiple arrivals with different speeds and directions. These are important attributes of the seismogram to know about before attempting to model waveform details for crustal structure.

Structure Modeling

The combination of a densely deployed seismic array, CWT denoising and array processing methods, and a well-controlled seismic source has allowed considerable detail to be discerned from waveforms that started out with a nominal SNR of less than one. It is unusual to observe such well-formed and coherent local seismic phases from events tens of kilometers from a station. The distinct Rayleigh wave dispersion determined for structure under the array (Figure 7) can be used to infer a velocity model that can find further use in locating nearby seismicity and understanding the propagation characteristics of local seismic wave trains.

Wave attributes inferred from an array reflect both the structure under the array and some of the history of wave propagation that the seismic wave experienced along the entire path. Rayleigh wave phase velocity inferred from the array analysis (Figure 7) is primarily related to the local structure under the array. However, the back-azimuth anomaly is an indication of wave propagation effects that occurred outside of the array. Group velocity, as it is usually measured, is a whole-path wave attribute since it is usually calculated by dividing the source-receiver distance by the group arrival time (e.g., Ewing et al., 1957; Capon, 1970). Lateral refraction due to horizontal velocity heterogeneity is governed by Snell's law and the phase velocity. Examining both phase and group velocity may offer clues to the structure causing lateral refraction and the differences in array structure compared to the whole path.

Using station 3016 as the central reference array station, group velocity was determined for both the local array structure and along the entire path. The Rayleigh waveforms obtained after scale-time gating over the 81 array stations were narrow bandpass filtered with a bandwidth of 0.125 Hz around central frequencies starting at 1 Hz with a frequency increment of 0.125 Hz. The envelope functions of the bandpassed Rayleigh waves were computed using the instantaneous amplitude of the analytic signal and the arrival time of the peaks of the envelopes were automatically picked. Group velocity for the whole path was estimated by dividing the source – receiver distance of 34.7 km at station 3016 by the envelope peak time. Group velocity under the array was determined by inverting the peak arrival times for group slowness in x (EW) and y (NS) (see Appendix A for details). Surprisingly, the group velocity data for the array could clearly discriminate between the great circle back azimuth and the group arrival back azimuth for frequencies less than 2 Hz (Figures 10 and 11). The whole-path group velocity and group velocity under the array were not significantly different suggesting that any horizontal structure changes may be subtle (Figure 11).

A smooth structure model was determined from the phase velocity measurements of Figure 7 with the addition of 4 lower frequency measurements using the entire 247 element Wavefields array (Figure 12). Measurements at 0.375, 0.5, 0.625, and 0.75 Hz were made in an attempt to constrain the structure deeper in the sedimentary column. The fundamental mode data were inverted using a simple velocity node model where the shear wave velocities at four nodes define the structure and velocity between the nodes are linearly interpolated except at the layer boundary (Appendix B). The depth of node 2 (at 0.6 km) was also the object of inversion. The thickness of the sedimentary column was constrained to be 1.7 km as determined from a nearby geotechnical well log (Figure 1). The results show that a very simple velocity structure can fit

the phase velocity data and that the data are most sensitive to the very near surface velocity gradient. This suggests that small changes in the near surface velocity could explain the back azimuth anomaly. A candidate structure is the roughly EW trending northern edge of the Salt Fork River plain (Figure 1b) where it could be expected that the river plain has somewhat lower shear wave velocities in the uppermost part of the structure compared to structure north of the river. A phase velocity contrast of 0.3 km/s could explain the back-azimuth anomaly for the 2Hz Rayleigh waves.

Source Parameters

Waveforms from the M3.6 28 June 2016 Langston, Oklahoma, earthquake offer an example for using CWT processing techniques to infer source parameters, particularly observations of earthquake depth phases (Figure 13). There is only a small amount of background noise and the waveforms show a distinctive set of body and surface waves. Herrmann (2016) derived a moment tensor model for this event using available regional broadband data that were filtered in the 0.03 to 0.1 Hz frequency band. The mechanism shows right-lateral strike-slip faulting occurring on a NE-SW vertical plane or left-lateral strike-slip motion on an 80° dipping NW-SE striking plane (Figure 1). Source depth was inferred to be 4 km.

These waveforms were processed using the CWT thresholding and block manipulation techniques to remove noise and then separate the various phases in the seismograms. The denoised vertical component scalograms show several prominent component phases including the fundamental mode Rayleigh wave, a harmonic and dispersed PL phase, along with high frequency P and associated coda (Figures 14 and 15).

Choosing a scale-time gate around the low scale (high frequency) portion of the P waveform yields a distinctive pair of phases that are seen to propagate at a velocity of 6.4 km/s (Figure 16). Source depth can be estimated from the relative time of 1s between the two phases if the second phase is interpreted as pP where

$$t_{pP} - t_P = 2\eta_\alpha h \quad (14)$$

for the relative time between P and pP or if the second phase is sP so that

$$t_{sP} - t_P = (\eta_\alpha + \eta_\beta) h \quad (15)$$

where $\eta_\alpha = \left(\frac{1}{\alpha^2} - p^2 \right)^{\frac{1}{2}}$, $\eta_\beta = \left(\frac{1}{\beta^2} - p^2 \right)^{\frac{1}{2}}$, α and β are the average P and S wave velocities

above the source, respectively, p is the horizontal slowness, and h is the source depth (Langston, 1987). Assuming the second phase is pP yields a source depth of 4.0km for average P and S velocities of 5.0km/s and 2.9km/s. If the phase is sP, then the source depth is 2.3km/s.

Array examination of the transverse component waveforms gives an estimate of 0.26 s/km for horizontal slowness of the initial 3s of the SH waveforms (Figure 16) and observations of a distinct secondary arrival that is interpreted as sS with a relative time of 2s, implying a source depth of 4.4 km. The pP and sS times suggest that the source depth is between 4 and 4.4km which is consistent with the regional moment tensor depth of 4km (Herrmann, 2016). The discrepancy between pP and sS estimates is probably due to unknowns in the near-source velocity structure. This suggests that knowledge of the wave attributes obtained by precise decomposition of the seismogram for component phases can significantly constrain the source depth. Source depth is very difficult to accurately constrain using standard earthquake location algorithms based on direct wave travel times for earthquakes within sparse networks or from relatively long-period moment tensor source inversion.

Discussion

The use of time-frequency representations of seismic signals literally offers another dimension to view and manipulate time series of interest. The techniques outlined here using the continuous wavelet transform can improve the ability to recognize those regions of the scale-time plane in the wavelet domain that contain high SNR portions of wanted seismic signals. Finding these high SNR data spaces is an important step towards optimizing a processing flow for detection and analysis of small seismic events in geographic regions of interest using seismic arrays. The additional capabilities of investigating the wave composition of seismograms by separating seismic phases through block manipulation is a useful tool for studying details of wave propagation and source excitation in phased array processing. It should also be helpful in understanding the structure effect when modeling data using synthetic seismograms.

Because using the CWT in seismological signal analysis is not commonplace, a typical question concerns the amount of distortion that noise thresholding and block manipulation might introduce in the filtered seismograms that could affect correlation across a phased array. The answer to this question is that “it depends”. Any signal processing method has limits. My experience with CWT techniques is that noise thresholding for high SNR portions of the scale-time plane does little to degrade time domain waveforms across a phased array. Denoised waveforms from the 2000lb explosion displayed in this paper showed very high correlation across the dense nodal array. Array beams using standard frequency-wavenumber methods and CWT beam forming often approached the theoretical beam response of the array showing that seismic phase waveforms were highly similar (e.g., Figures 9 and 16). However, I tried the same analysis for the 250lb shot near the shotpoint of the 2000lb explosion with negative results. Signal for the smaller explosion was comparable to the noise, even in that part of the scale-time

plane where the 2000lb shot had high SNR, so that soft thresholding removed both signal and noise. It can be expected that signal distortion will occur from thresholding when the SNR is relatively low and not much greater than one (1).

Likewise, care should be taken when performing the signal decomposition step to separate seismic phases. A polygon can be arbitrarily drawn around any area on the scale-time plane of a signal. Clipping out an arbitrary portion of the CWT will yield a time domain waveform that could look interesting but be completely meaningless in terms of reflecting some aspect of real wave propagation. Signal decomposition should be based on robust features of the CWT that have high energy and distinct attributes that isolate the feature from others. This is in keeping with the philosophy of “sparsity” (Starck et al., 2010) where an attempt is made to describe a signal with the minimum amount of information. A classic Fourier example is the description of a long duration time domain sinusoid by its single frequency in the frequency domain. In the case of the explosion Rayleigh wave phases observed here, the fundamental mode portion of the seismogram was generally separate from other portions of the CWT on the scale-time plane and showed dispersion through decreasing scale with time. Perhaps a better way to think about the phase decomposition analysis is that it is a hypothesis test where the hypothesis, the separated signal, is analyzed by other means to test its usefulness. However, there is no doubt that scalograms of interesting signals have similar attributes as seen across a phased array. This alone suggests that these new signal attributes could be incorporated into pattern recognition or machine learning algorithms.

Signal decomposition using CWT methods will also help in a common problem encountered in wave gradiometry. A geodetic array (Spudich et al., 1995) is a variant of a phased array where the array aperture is a small fraction of the target wavelength. Provided that there are a

sufficient number of elements of the array that have matching instrument responses, wave attributes are inferred by estimating wave spatial gradients by representing the observed local wavefield in terms of a Taylor's series in displacement. The inferred first order spatial gradients are, of course, the strains and rotations induced by wave motion under the array. The spatial gradients are related to the time gradient (velocity) through the wave equation so that wave horizontal slowness, azimuth of propagation, and other attributes can be estimated directly from amplitudes (Langston, 2007a; b; c; Langston and Liang, 2008). A central assumption in the method is that a single wave is the object of analysis. Obviously, this may not be true for arbitrary wavefields. Being able to separate waves in a seismogram using the CWT and block manipulation has the potential to improve gradiometry wave attributes since the disrupting effects of wave interference can be minimized. This is the subject of ongoing work.

Conclusions

Phased array processing can benefit from application of CWT denoising and block manipulation techniques. Noise thresholding on the scale-time plane can be used to find high SNR parts of the CWT spectrum of a signal that can be further studied using standard frequency-wavenumber beamforming. Array seismograms can be separated into component phases using scale-time gating where specific seismic phase blocks in the CWT domain are correlated from a reference station to all other stations in the array. The separated seismic phases can then be analyzed using standard techniques or by constructing array beams by directly using the CWT.

These techniques were used on explosion data recorded by the 2016 IRIS Wavefields experiment to determine Rayleigh wave phase velocity and group velocity dispersion under a cross-shaped subarray. The 1-3Hz Rayleigh waves display horizontal refraction along the wave

path from source to array and were used to develop a shallow velocity model for the upper 1.7km. In addition, near-source pP and sS reflections were detected in seismograms from a M3.6 local earthquake to constrain source depth to 4 to 4.4 km, consistent with a previously determining regional moment tensor model of the earthquake.

Data and Resources

Data from the IRIS Wavefields Experiment are available from the IRIS Data Management Center (Anderson, 2016). I gratefully acknowledge the use GMT (Wessel and Smith, 1998) and Seismic Analysis Code (Goldstein et al., 2003) software in this work.

Acknowledgements

This work was supported by the Air Force Research Laboratory under contract #FA9453-18-C-0064 which is gratefully acknowledged.

482 **References**

- 483 Abrahamson, N. A., B. A. Bolt, R. B. Darragh, J. Penzien, and Y.B. Tsai (1987). The SMART-I
484 accelerograph array (1980-1987): A review. *Earthquake Spectra*, 3, 263-287.
- 485 Aki, K., and P. G. Richards (1980). *Quantitative Seismology - Theory and Methods*. San
486 Francisco, CA: W. H. Freeman and Co.
- 487 Al-Shukri, H., G. L. Pavlis, and F. L. Vernon (1995). Site effect observations from broadband
488 arrays. *Bull. Seism. Soc. Am.*, 85, 1785-1769.
- 489 Anderson, J. S. K. (2016). *IRIS Community wavefield experiment in Oklahoma*. Retrieved from
490 https://doi.org/10.7914/SN/YW_2016.
- 491 Aster, R. C., B. Borchers, and C. H. Thurber (2005). *Parameter estimation and inverse*
492 *problems*, Elsevier, Inc.
- 493 Brocher, T. M. (2005). Empirical relations between elastic wavespeeds and density in the Earth's
494 crust, *Bull. Seism. Soc. Am.*, 95, 2081-2092, doi 10.1785/0120050077.
- 495 Capon, J. (1969). High resolution frequency-wavenumber spectrum analysis. *Proc. IEEE*, 57,
496 1408-1418.
- 497 Capon, J. (1970). Analysis of Rayleigh-wave multipath propagation at LASA. *Bull. Seism. Soc.*
498 *Am.*, 60, 1701-1731.
- 499 Capon, J., R. J. Greenfield, and R. J. Kolker, R. J. (1967). Multidimensional maximum
500 likelihood processing of a large aperture seismic array. *Proc. IEEE*, 55, 192-211.
- 501 Claassen, J. P. (1985). Design criteria for sizing regional arrays. In A. U. Kerr (Ed.), *The VELA*
502 *Program: A Twenty-Five Year Review of Basic Research* (pp. 506-515). United States:
503 Dianne L. Carlson.

504 Constable, S. C., R. L. Parker, and C. G. Constable (1987). Occam's inversion: a practical
505 algorithm for generating smooth models from electromagnetic sounding data,
506 *Geophysics*, 52, 289-300.

507 Douglas, A. (2002). Seismometer arrays - their use in earthquake and test ban seismology. In W.
508 H. K. Lee, H. Kanamori, P. C. Jennings, & C. Kisslinger (Eds.), *International Handbook*
509 *of Earthquake and Engineering Seismology* (pp. 357-367). San Diego, California:
510 Academic Press.

511 Filson, J. (1975). Array seismology. *Annual Review of Earth and Planetary Sciences*, 3, 157-181.
512 doi:10.1146/annurev.ea.03.050175.001105

513 Gibbons, S. J. (2014). The applicability of incoherent array processing to IMS seismic arrays.
514 *Pure Appl. Geophys.*, 171, 377-394. doi:10.1007/s00024-012-0613-2

515 Gibbons, S. J., J. Schweitzer, R. Ringdal, T. Kväerna, S. Mykkeltveit, and B. Paulsen (2011).
516 Improvements to seismic monitoring of the European Arctic using three-component array
517 processing at SPITS. *Bull. Seism. Soc. Am.*, 101, 2737-2754. doi:10.1785/01201100109

518 Goldstein, P. and R. J. Archuleta (1987). Array analysis of seismic signals. *Gephys. Res. Lett.*,
519 14, 13-16.

520 Goldstein, P., D. Dodge, and M. Firpo (2003). SAC2000: Signal processing and analysis tools
521 for seismologists and engineers. In W. H. K. Lee, H. Kanamori, P. C. Jennings, & C.
522 Kisslinger (Eds.), *IASPEI International Handbook of Earthquake and Engineering*
523 *Seismology*. London: Academic Press.

524 Grossmann, A., R. Kronland-Martinet, and J. Morlet (1989). Reading and understanding the
525 continuous wavelet transform. In J. Combes, A. Grossmann, & P. Tchamitchian (Eds.),
526 *Wavelets: Time-Frequency Methods and Phase-Space* (pp. 2-10). New York: Springer.

527 Gupta, I. N., C. S. Lynnes, T. W. McElfresh, and R. A. Wagner (1990). F-k analysis of NORESS
528 array and single-station data to identify sources of near-receiver and near-source
529 scattering. *Bull. Seism. Soc. Am.*, 80, 2227-2241.

530 Harkrider, D. G. (1964). Surface waves in multilayered elastic media: I. Rayleigh ad Love waves
531 from buried sources in a multilayered elastic half-space. *Bull. Seism. Soc. Am.*, 54, 627-
532 679.

533 Harris, D. B. and T. Kværna (2010). Superresolution with seismic arrays using empirical
534 matched field processing. *Geophy. J. Int.*, 182, 1455-1477. doi:10.1111/j.1365-
535 246x.2010.04684.x

536 Haubrich, R. A. (1968). Array Design. *Bull. Seis. Soc. Am.*, 58(3), 977-991.

537 Havskov, J. and G. Alguacil (2004). *Instrumentation in Earthquake Seismology*: Springer.

538 Herrmann, R. (2016).
539 http://www.eas.slu.edu/eqc/eqc_mt/MECH.NA/20160628195756/index.html, last
540 accessed December 7, 2020.

541 Kushnir, A. F. (1996). Algorithms for adaptive statistical processing of seismic array data. In E.
542 S. Husebye & A. M. Dainty (Eds.), *Monitoring a Comprehensive Test Ban Treaty* (pp.
543 565-586). Netherlands: Kluwer Academic Publishers.

544 Kværna, T. (1989). On exploitation of small-aperture NORESS type arrays for enhanced P-wave
545 detectability. *Bull. Seis. Soc. Am.*, 79, 888-900.

546 Kværna, T. and F. Ringdal (1992). Integrated array and three-component processing using a
547 seismic microarray. *Bull. Seis. Soc. Am.*, 82, 870-882.

548 Langston, C. A. (1987). Depth of faulting during the 1968 Meckering, Australia, earthquake
 549 sequence determined from waveform analysis of local seismograms. *J. Geophys. Res.*,
 550 92, 11561-11574.

551 Langston, C. A. (2007a). Spatial gradient analysis for linear seismic arrays. *Bull. Seism. Soc.*
 552 *Am.*, 97, 265-280. doi:10.1785/0120060100

553 Langston, C. A. (2007b). Wave Gradiometry in the time domain. *Bull. Seism. Soc. Am.*, 97, 926-
 554 933. doi:10.1785/0120060152

555 Langston, C. A. (2007c). Wave Gradiometry in two dimensions. *Bull. Seism. Soc. Am.*, 97, 401-
 556 416. doi:10.1785/0120060138

557 Langston, C. A. and C. Liang (2008). Gradiometry for polarized seismic waves. *Jour. Geophys.*
 558 *Res.*, 113. doi:doi:10.1029/2007JB005486

559 Langston, C. A. and S. M. Mousavi (2019). Separating signal from noise and from other signal
 560 using nonlinear thresholding and scale-time windowing of continuous wavelet
 561 transforms. *Bull Seism. Soc. Am.*, 109, 1691-1700. doi:10.1785/0120190073

562 Lindfors, A. (1996). Array processing by phase regression. In E. S. Husebye & A. M. Dainty
 563 (Eds.), *Monitoring a Comprehensive Test Ban Treaty* (pp. 629-644). Netherlands: Kluwer
 564 Academic Publishers.

565 Mykkeltveit, S. (1985). A new regional array in Norway: design work and results from analysis
 566 of data from a provisional installation. In A. U. Kerr (Ed.), *The VELA Program, A Twenty*
 567 *Five Year Review of Basic Research* (pp. 546-553).

568 Mykkeltveit, S., K. Astebol, D. J. Doornbos, and E. S. Husebye (1983). Seismic array
 569 configuration optimization. *Bull. Seism. Soc. Am.*, 73, 173-186.

570 Nawab, S., F. Dowla, and R. Lacoss (1985). Direction determination of wideband signals. *IEEE*
571 *Trans. Acous. Speech Sig. Proc.*, 33, 1114-1122.

572 Rost, S. and C. Thomas (2002). Array seismology: methods and applications. *Rev. Geophys.*, 40.
573 doi:10.1029/2000RG000100

574 Spudich, P., L. K. Steck, M. Hellweg, J. B. Fletcher, and L. M. Baker (1995). Transient stresses
575 at Parkfield, California, produced by the M7.4 Landers earthquake of June 28, 1992:
576 Observations from the UPSAR dense seismograph array. *Jour. Geophys. Res.*, 100, 675-
577 690.

578 Starck, J.-L., F. Murtagh, and J. M. Fadili (2010). *Sparse Image and Signal Processing*. New
579 York: Cambridge University Press.

580 Stump, B., M. Jubn, C. Hayward, J. Jeon, I.-Y. Che, K. Thomason, S. M. House, and J.
581 McKenna, J. (2004). Small Aperture Seismo-Acoustic Arrays: Design, Implementation
582 and Utilization. *Bull. Seism. Soc. Am*, 94, 220-236.

583 Sweet, J. R., K. R. Anderson, S. Bilek, M. Brudzinski, X. Chen, H. DeShon, C. Hayward, M.
584 Karplus, K. Keranen, C. Langston, F.-C. Lin, M. B. Magnani, and R. L. Woodward
585 (2018). A community experiment to record the full seismic wavefield in Oklahoma.
586 *Seism. Res. Lett.*, 89, 1923-1930. doi:10.1785/0220180079

587 Toksoz, M. N., A. M. Dainty, and E. E. Charette (1991). Coherency of ground motions at
588 regional distances and scattering. *Phys. Earth and Planet. Int.*, 67, 162-179.

589 Wagner, G. S. and T. J. Owens (1993). Broadband bearing-time records of three-component
590 seismic array data and their application to the study of local earthquake coda. *Geophys.*
591 *Res. Lett.*, 20, 1823-1826.

592 Wessel, P. and W. H. F. Smith (1998). New, improved version of Generic Mapping Tools
593 released. *EOS, Trans. Amer. Geophys. U.*, 79, 579.

594

595 **Affiliation**

596 Center for Earthquake Research and Information

597 University of Memphis

598 3876 Central Ave., Suite 1

599 Memphis, TN 38152

600

601

Figure Captions

Figure 1 – (a) Regional index map for Oklahoma and surrounding states. Location of the IRIS Wavefields experiment is shown by the star, cities by filled squares, and sources with filled circles. The focal mechanism of the M3.6 Langston, Oklahoma, earthquake shows largely strike-slip motion (Herrmann, 2016). (b) shows a smaller scale map of topography around the IRIS experiment, shot point 1 for the AFTAC explosion experiment, the location of the Kirk borehole which was logged for acoustic velocity, and stations of the IRIS YW array. Red dots denote locations of the 5Hz nodal instruments. The 6 tripartite clusters show the location of broadband instrumentation for the Golay 3x6 array and the dark cross denote the cross array stations used in this paper. The great circle path is drawn from the AFTAC shotpoint to the center of the cross array. The yellow line is the inferred position of the northern boundary of the Salt Fork River valley that may represent a horizontal velocity boundary. One possible ray path is drawn between the shotpoint and array that explains the back azimuth anomaly for 2Hz fundamental mode Rayleigh waves observed at the array.

Figure 2 – Array geometry (left) and co-array diagram (right) of the cross array constructed from a subset of the IRIS experiment. Positions for stations 3016 and 3001 are shown on the array diagram. The co-array is a plot of all distances and azimuths between every pair of stations in the array and is an indicator of how well a seismic wavelength is sampled in space.

Figure 3 – This is an example of scale-time gating the fundamental mode Rayleigh wave from denoised explosion vertical component seismograms of two stations of the cross array. Panel (a) shows the denoised seismogram (bottom) and its scalogram (top) after performing the

Continuous Wavelet transform. A polygon is manually picked to isolate the fundamental mode energy on the scalogram at the reference station 3016. This portion of the scalogram is clipped out and then correlated with the scalograms of all other stations in the array. Panel (b) shows the shifted polygon encompassing the Rayleigh wave at station 3001. (c) shows the amplitude of the correlation vs time shift between the stations. The peak of the correlation occurs at an advanced time, relative to 3016, since station 3001 is closer to the source.

Figure 4 – Panel (a) shows the scale-time gated Rayleigh waves obtained for stations of the cross array. Panel (b) is the broadband frequency-wavenumber result for the frequency band of 1 to 3 Hz encompassing the bandwidth of the Rayleigh waves. The small x's show the results of narrow band f-k for phase velocity as a function of frequency. Note that the bulk of the Rayleigh wave energy arrives approximately 10 degrees clockwise from the expected great circle path shown by the black line.

Figure 5 – This figure illustrates two methods for scale-time gating the low scale/high frequency P wave train. The top panel (a) shows a choice of a block on the scalogram the encompasses the desired portion of the waveform. Panel (b) shows its complement where a block containing the high amplitude modes are chosen for correlation instead. (c) displays the seismogram at the reference station 3016. P1 and P2 body wave phases are annotated.

Figure 6 – Results of scale-time gating using the two different choices of CWT blocks shown in Figure 5. In (a), the P wave block in Figure 5a was used to correlate with all other station

CWTs. However, results for some stations, shown by the delimited rectangular areas, were poor because the reference CWT block had higher correlation values with later arriving, high-amplitude modes. (b) This was alleviated by correlating with the modes block (Figure 5b) then removing this part of the CWT before inverse transforming.

Figure 7 – Results of Rayleigh wave phase velocity dispersion analysis using narrow band f-k.

(a) Slowness as a function of frequency. (b) Phase velocity as a function of frequency. (c) Back azimuth as a function of frequency. The heavy line at 311° is the theoretical great circle backazimuth. (d) Selected slowness spectra plots for the frequencies denoted by arrows. (e) Theoretical array responses for the corresponding plots shown in (d). Note that f-k spectra show the effects of Rayleigh wave multipathing for frequencies greater than 2.5Hz. f-k spectra display multiple peaks at different backazimuths and slownesses.

Figure 8 – f-k spectra of P1 (left) and P2 (right) phases in the vertical components of the 2000lb explosion. Note the narrow beams showing that phases are highly correlated across the array.

Figure 9 – CWT beamforming result for the P wave block of the 2000lb AFTAC explosion. The low scale wavetrain was determined from excluding the modes block (Figures 5b, 6b).

Additionally, a scale bandpass of 0.1 to 0.5s was performed and is shown in (a). P1, P2, S, and Coda phases are annotated. (b) and (c) show the inferred phase velocity and backazimuth, respectively, at every 10^{th} time point in the trace. Red symbols denote well-

formed single CWT beams with $R \geq 0.5$ and blue for $R < 0.5$. Representative slowness beams are indicated for the times shown by vertical lines.

Figure 10 – Array group velocity analysis example for 1.375Hz vertical component Rayleigh waves. Group arrival times are plotted against station distance from the source assuming the great circle path to the source in (a). Because the waves are arriving from an azimuth clockwise from the great circle backazimuth, times from the two linear arms of the cross array are inconsistent. In (b), an inversion for group slowness and backazimuth is performed to find the optimum backazimuth and group velocity for structure under the array (see Appendix A). The data clearly indicate that Rayleigh waves arrive 22° clockwise from the great circle backazimuth, similar to the amount seen in the phase velocity determination.

Figure 11 – (a) compares the group velocity determined by array analysis (filled circles) with the whole path group velocity determined by dividing the great circle distance by the group arrival time at station 3016 (filled squares). There seems to be no significant difference in group velocities determined by two independent means. (b) shows the backazimuth determined from the array group velocity analysis as a function of frequency. Multipathing causes the larger errors at frequencies greater than 2.5 Hz.

Figure 12 – (a) Velocity model determined from formal inversion of the phase velocity data. (b) Phase velocity data, data errors, and fit (line).

Figure 13 – Waveforms recorded at station 3016 for the M3.6 6/28/2016 Langston, Oklahoma, earthquake. Vertical, radial, and transverse component waveforms are shown. The data have been corrected for instrument response. P, PL, Rayleigh, and Love waves are annotated.

Figure 14 – Scale-time gates chosen for the vertical component of the M3.6 earthquake. The top panel shows the scalogram for the seismogram shown below. Time gate polygons were chosen for the low scale portion of the P wave and harmonic portion of the PL phase. S, Rg, and Coda phases are also annotated.

Figure 15 – Results from scale-time gating the vertical component of station 3016 using the P and PL wave gates shown in Figure 16. The original data is shown in the top panel and the gated waveforms shown below.

Figure 16 – (a) shows the gated P wave at the 81 stations of the cross array. The broadband f-k beam for 5 to 20Hz is shown in (b) and indicates that the two major phases, denoted by P and pP, have identical slownesses. (c) shows the instrument-corrected SH waves at the cross array with (c) the 1 to 10Hz broadband f-k response. S and sS phases are shown on the seismograms.

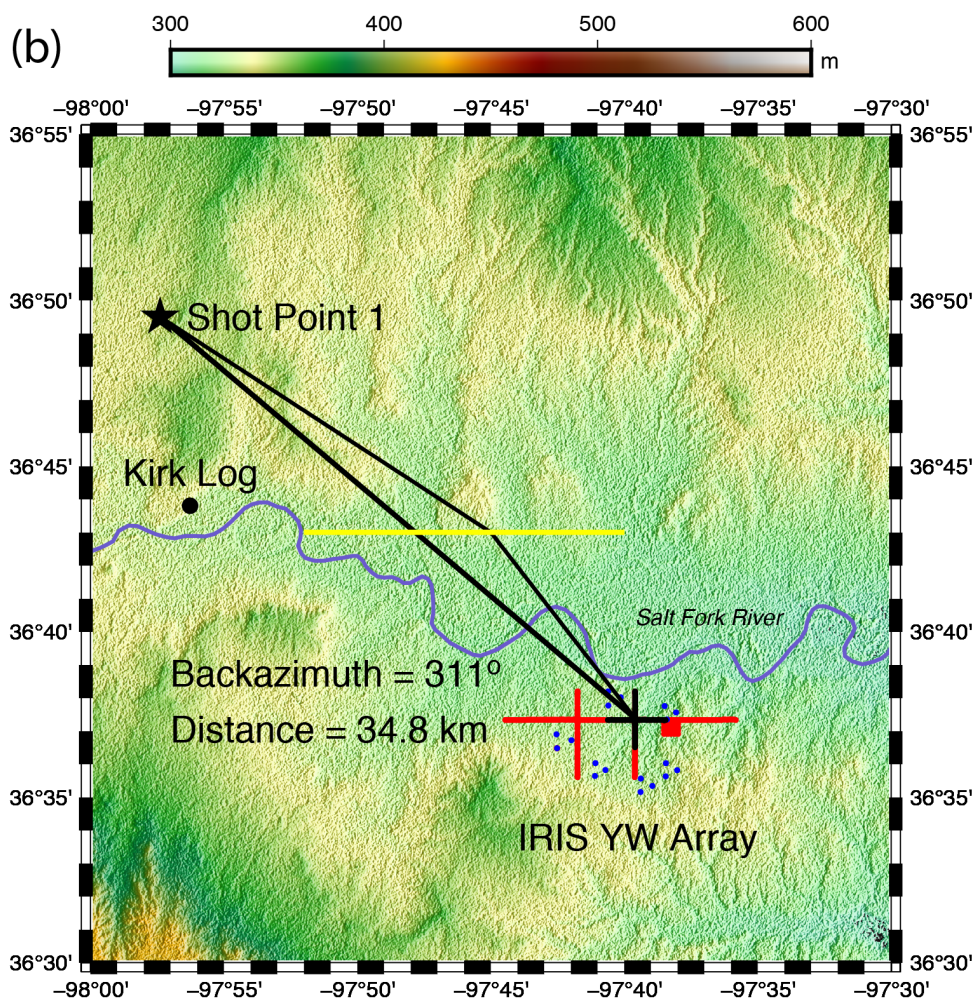
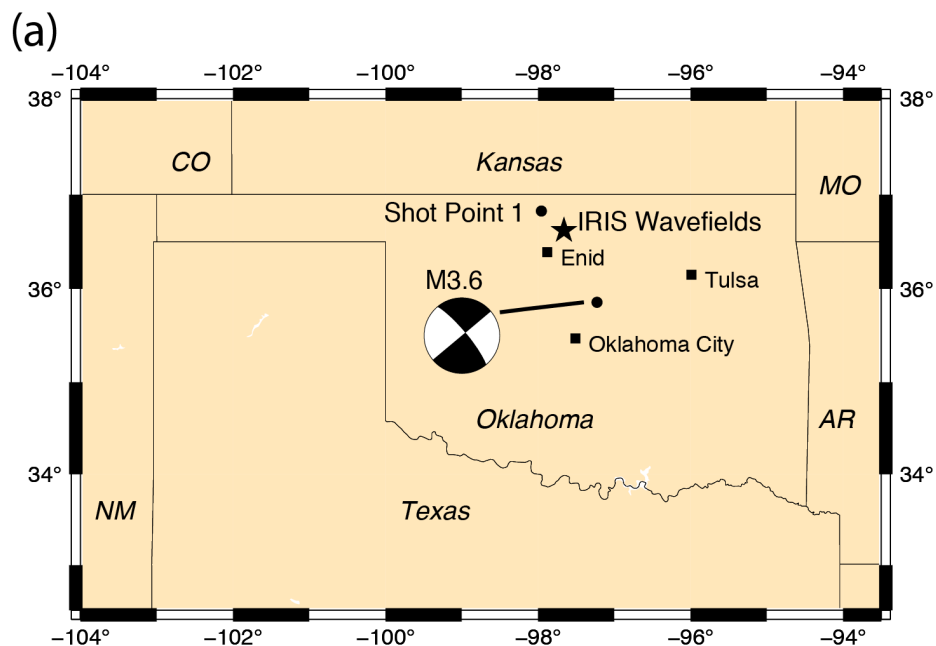


Figure 1 – (a) Regional index map for Oklahoma and surrounding states. Location of the IRIS Wavefields experiment is shown by the star, cities by filled squares, and sources with filled circles. The focal mechanism of the M3.6 Langston, Oklahoma, earthquake shows largely strike-slip motion (Herrmann, 2016). (b) shows a smaller scale map of topography around the IRIS experiment, shot point 1 for the AFTAC explosion experiment, the location of the Kirk borehole which was logged for acoustic velocity, and stations of the IRIS YW array. Red dots denote locations of the 5Hz nodal instruments. The 6 tripartite clusters show the location of broadband instrumentation for the Golay 3x6 array and the dark cross denote the cross array stations used in this paper. The great circle path is drawn from the AFTAC shotpoint to the center of the cross array. The yellow line is the inferred position of the northern boundary of the Salt Fork River valley that may represent a horizontal velocity boundary. One possible ray path is drawn between the shotpoint and array that explains the back azimuth anomaly for 2Hz fundamental mode Rayleigh waves observed at the array.

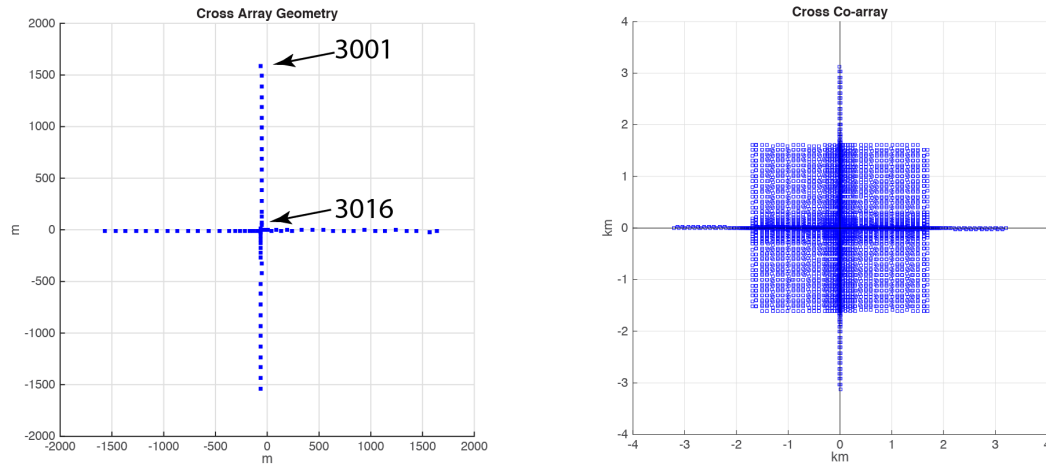


Figure 2 – Array geometry (left) and co-array diagram (right) of the cross array constructed from a subset of the IRIS experiment. Positions for stations 3016 and 3001 are shown on the array diagram. The co-array is a plot of all distances and azimuths between every pair of stations in the array and is an indicator of how well a seismic wavelength is sampled in space.

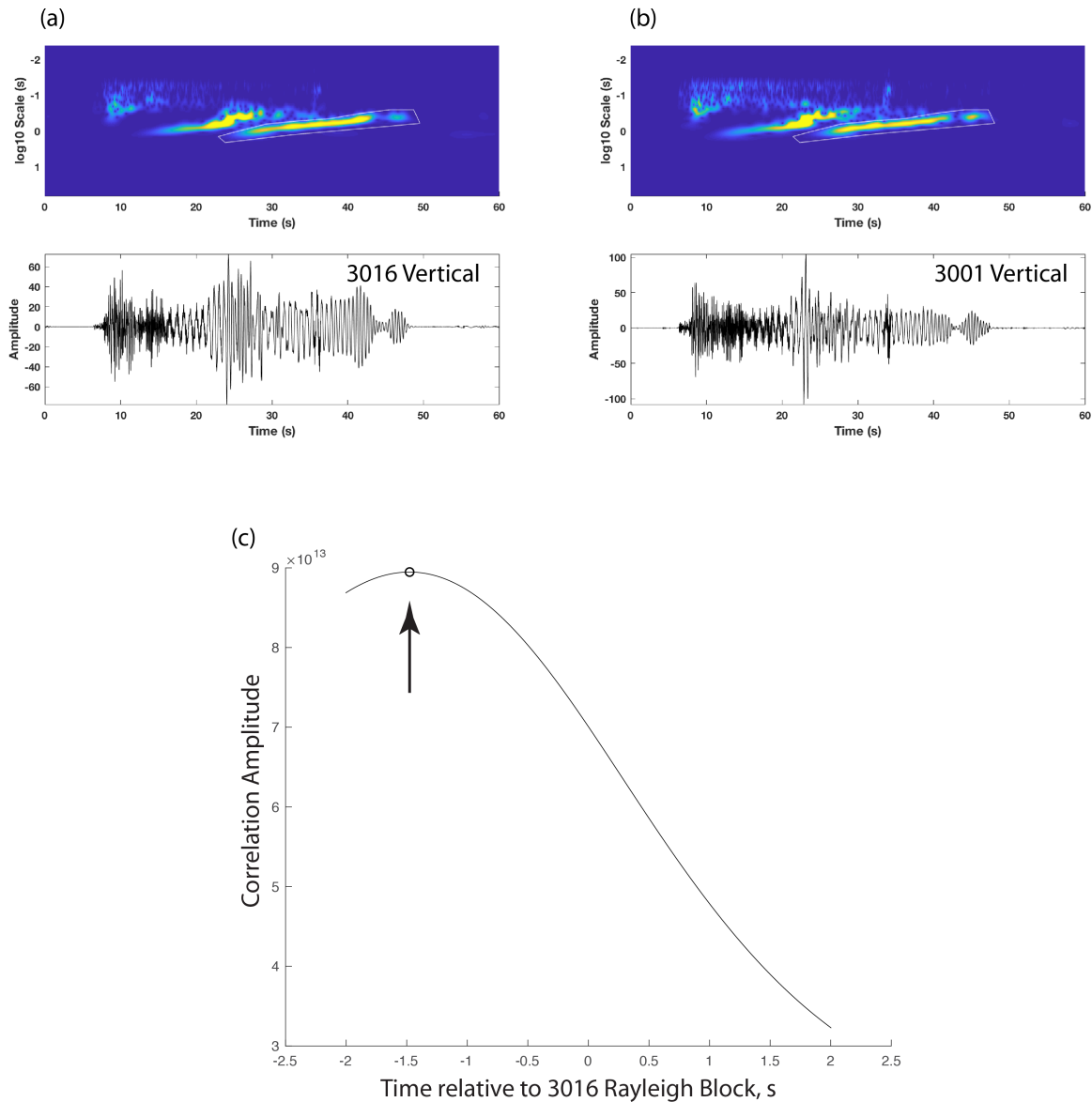
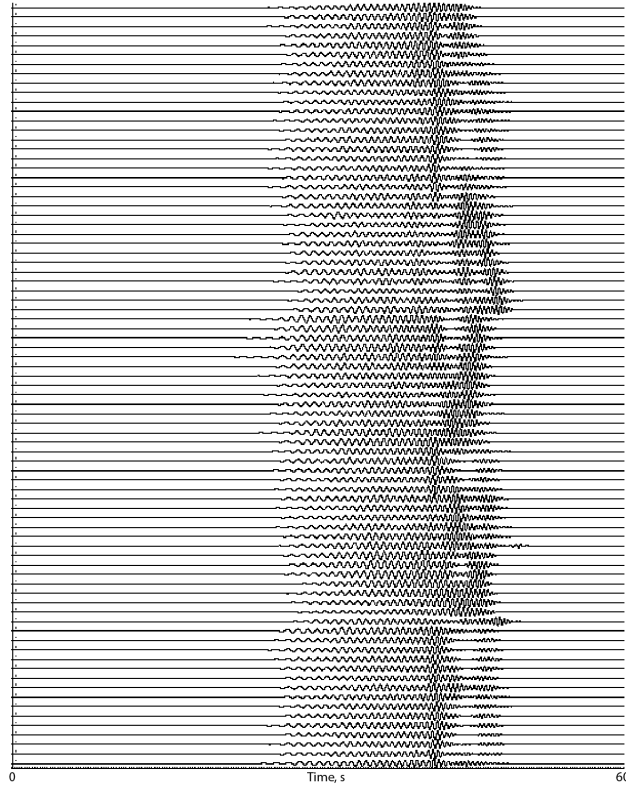


Figure 3 – This is an example of scale-time gating the fundamental mode Rayleigh wave from denoised explosion vertical component seismograms of two stations of the cross array. Panel (a) shows the denoised seismogram (bottom) and its scalogram (top) after performing the Continuous Wavelet transform. A polygon is manually picked to isolate the fundamental mode energy on the scalogram at the reference station 3016. This portion of the scalogram is clipped out and then correlated with the scalograms of all other stations in the array. Panel (b) shows the shifted polygon encompassing the Rayleigh wave at station 3001. (c) shows the amplitude of the correlation vs time shift between the stations. The peak of the correlation occurs at an advanced time, relative to 3016, since station 3001 is closer to the source.

(a)



(b)

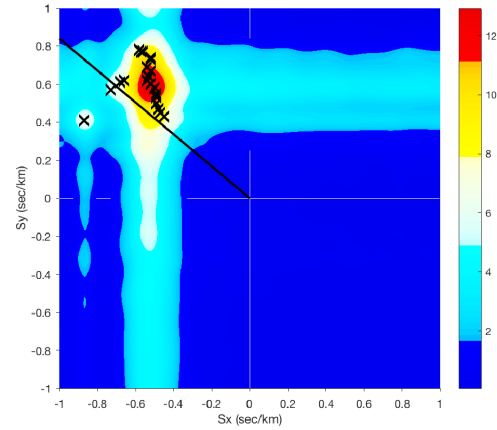


Figure 4 – Panel (a) shows the scale-time gated Rayleigh waves obtained for stations of the cross array. Panel (b) is the broadband frequency-wavenumber result for the frequency band of 1 to 3 Hz encompassing the bandwidth of the Rayleigh waves. The small x's show the results of narrow band f-k for phase velocity as a function of frequency. Note that the bulk of the Rayleigh wave energy arrives approximately 10 degrees clockwise from the expected great circle path shown by the black line.

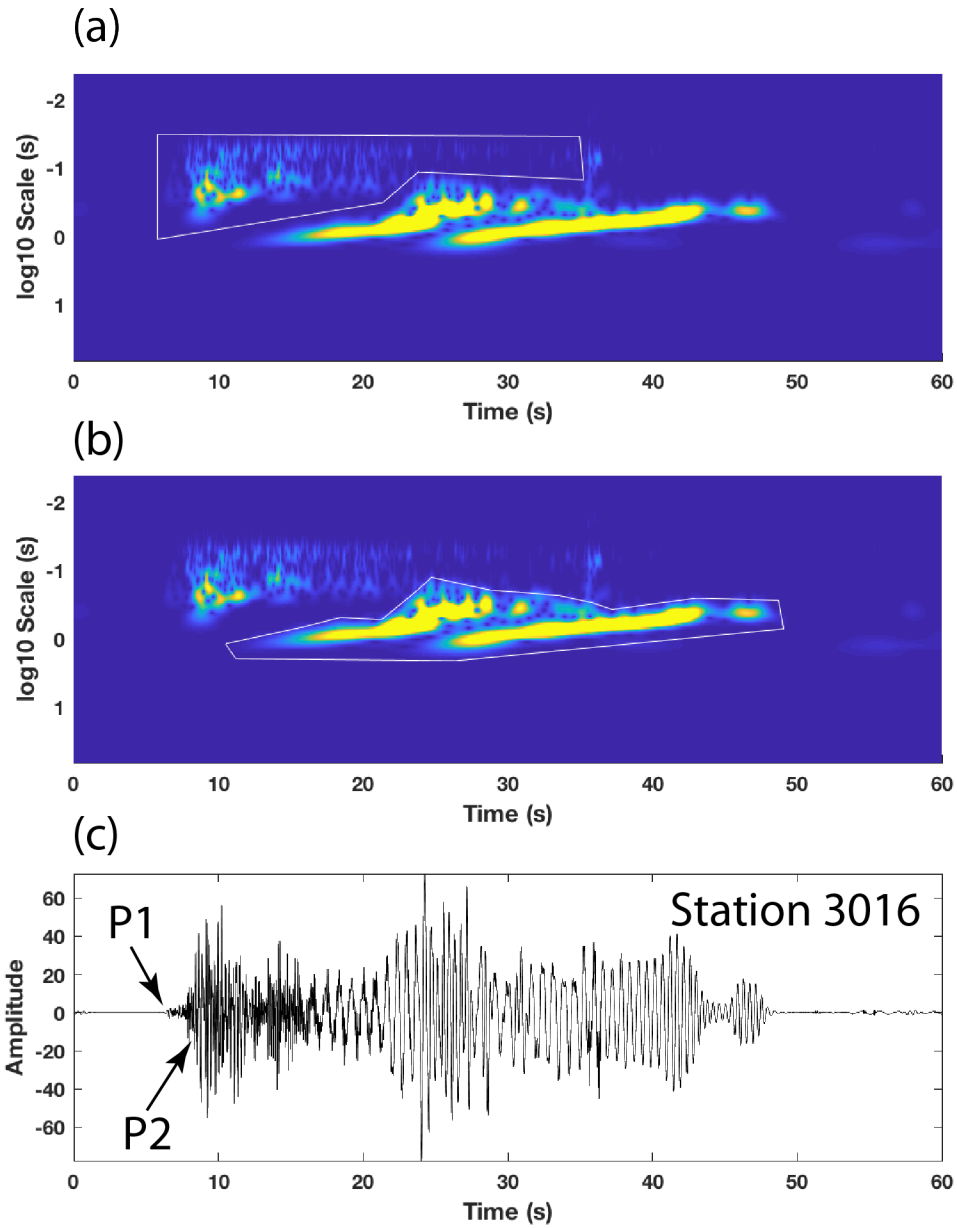


Figure 5 – This figure illustrates two methods for scale-time gating the low scale/high frequency P wave train. The top panel (a) shows a choice of a block on the scalogram the encompasses the desired portion of the waveform. Panel (b) shows its complement where a block containing the high amplitude modes are chosen for correlation instead. (c) displays the seismogram at the reference station 3016. P1 and P2 body wave phases are annotated.

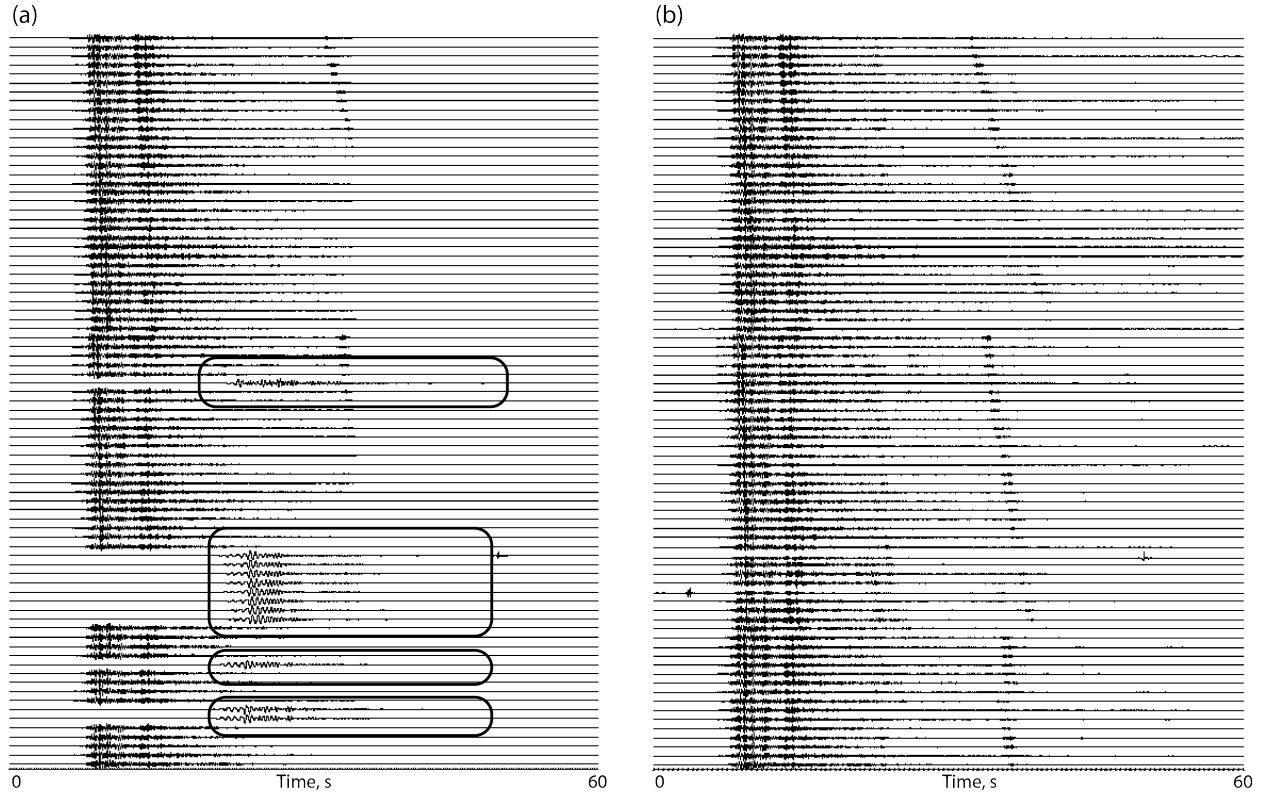


Figure 6 – Results of scale-time gating using the two different choices of CWT blocks shown in Figure 5. In (a), the P wave block in Figure 5a was used to correlate with all other station CWTs. However, results for some stations, shown by the delimited rectangular areas, were poor because the reference CWT block had higher correlation values with later arriving, high-amplitude modes. (b) This was alleviated by correlating with the modes block (Figure 5b) then removing this part of the CWT before inverse transforming.

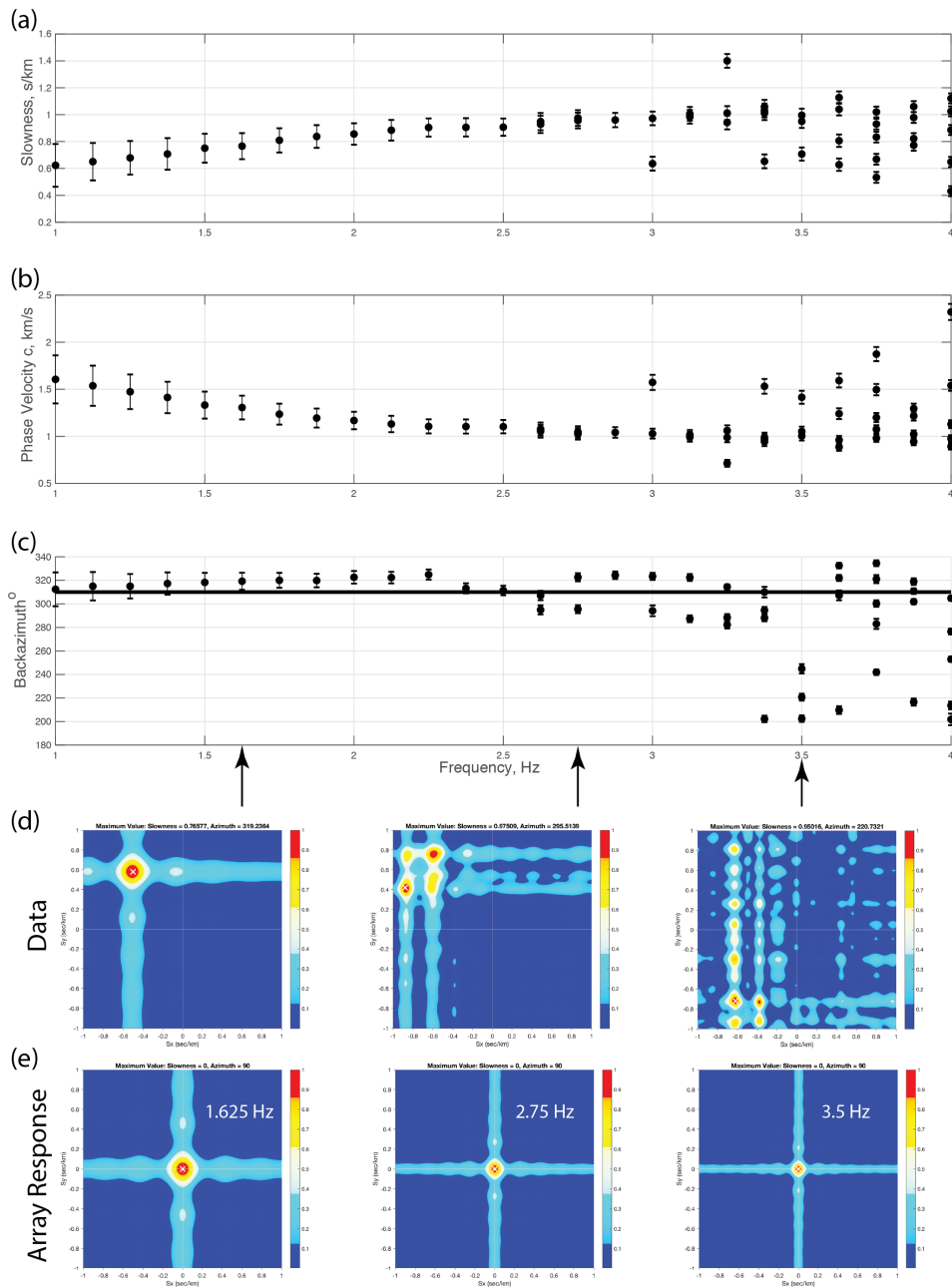


Figure 7 – Results of Rayleigh wave phase velocity dispersion analysis using narrow band f-k. (a) Slowness as a function of frequency. (b) Phase velocity as a function of frequency. (c) Back azimuth as a function of frequency. The heavy line at 311 $^\circ$ is the theoretical great circle backazimuth. (d) Selected slowness spectra plots for the frequencies denoted by arrows. (e) Theoretical array responses for the corresponding plots shown in (d). Note that f-k spectra show the effects of Rayleigh wave multipathing for frequencies greater than 2.5Hz. f-k spectra display multiple peaks at different backazimuths and slownesses.

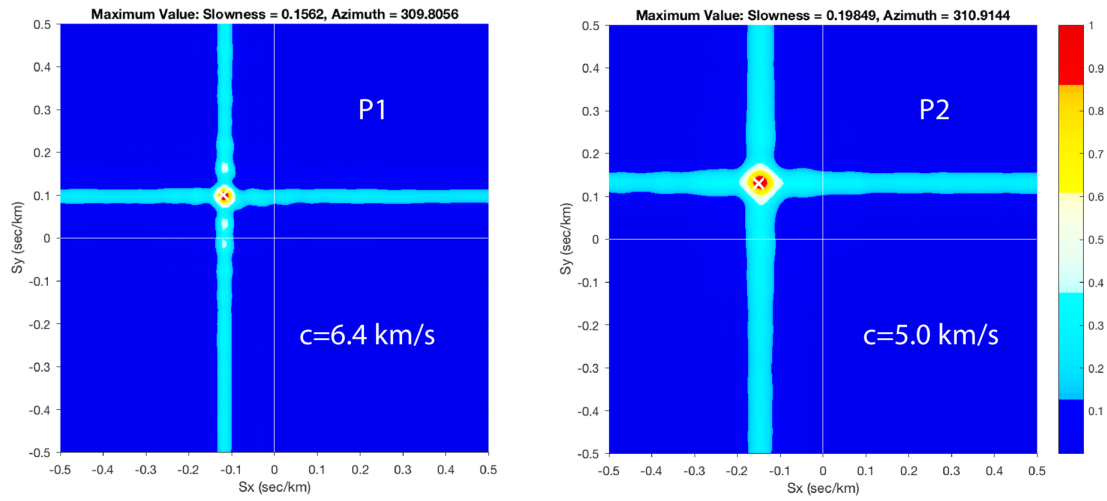


Figure 8 – f-k spectra of P1 (left) and P2 (right) phases in the vertical components of the 2000lb explosion. Note the narrow beams showing that phases are highly correlated across the array.

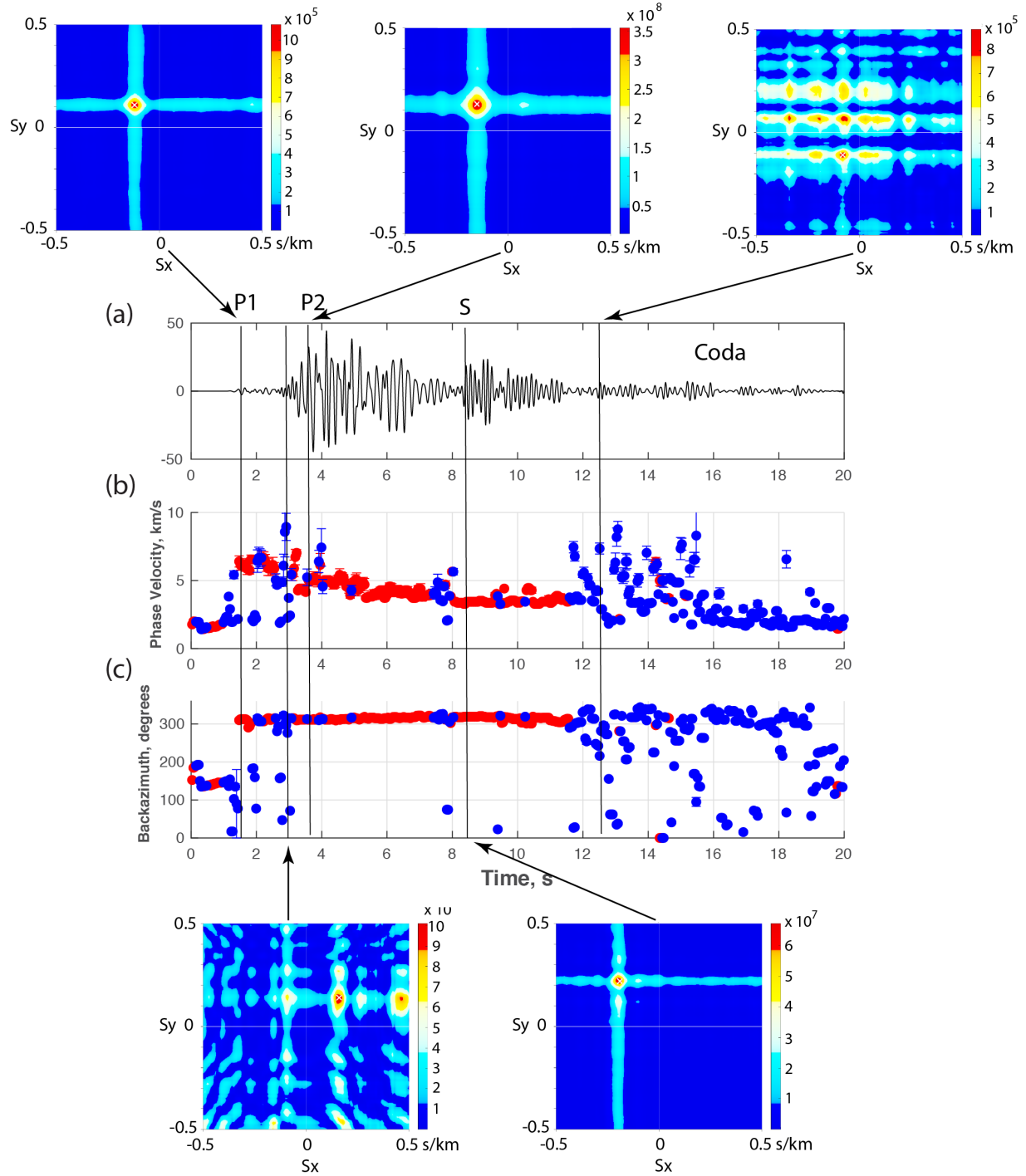


Figure 9 – CWT beamforming result for the P wave block of the 2000lb AFTAC explosion. The low scale wavetrain was determined from excluding the modes block (Figures 5b, 6b). Additionally, a scale bandpass of 0.1 to 0.5s was performed and is shown in (a). P1, P2, S, and Coda phases are annotated. (b) and (c) show the inferred phase velocity and backazimuth, respectively, at every 10th time point in the trace. Red symbols denote well-formed single CWT beams with $R \geq 0.5$ and blue for $R < 0.5$. Representative slowness beams are indicated for the times shown by vertical lines.

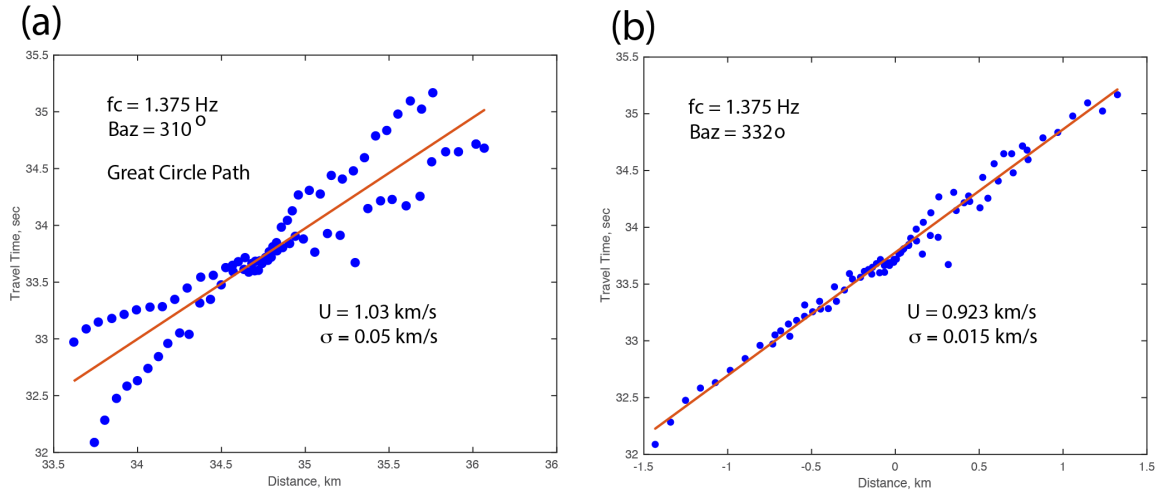


Figure 10 – Array group velocity analysis example for 1.375Hz vertical component Rayleigh

waves. Group arrival times are plotted against station distance from the source assuming the great circle path to the source in (a). Because the waves are arriving from an azimuth clockwise from the great circle backazimuth, times from the two linear arms of the cross array are inconsistent. In (b), an inversion for group slowness and backazimuth is performed to find the optimum backazimuth and group velocity for structure under the array (see Appendix A). The data clearly indicate that Rayleigh waves arrive 22° clockwise from the great circle backazimuth, similar to the amount seen in the phase velocity determination.

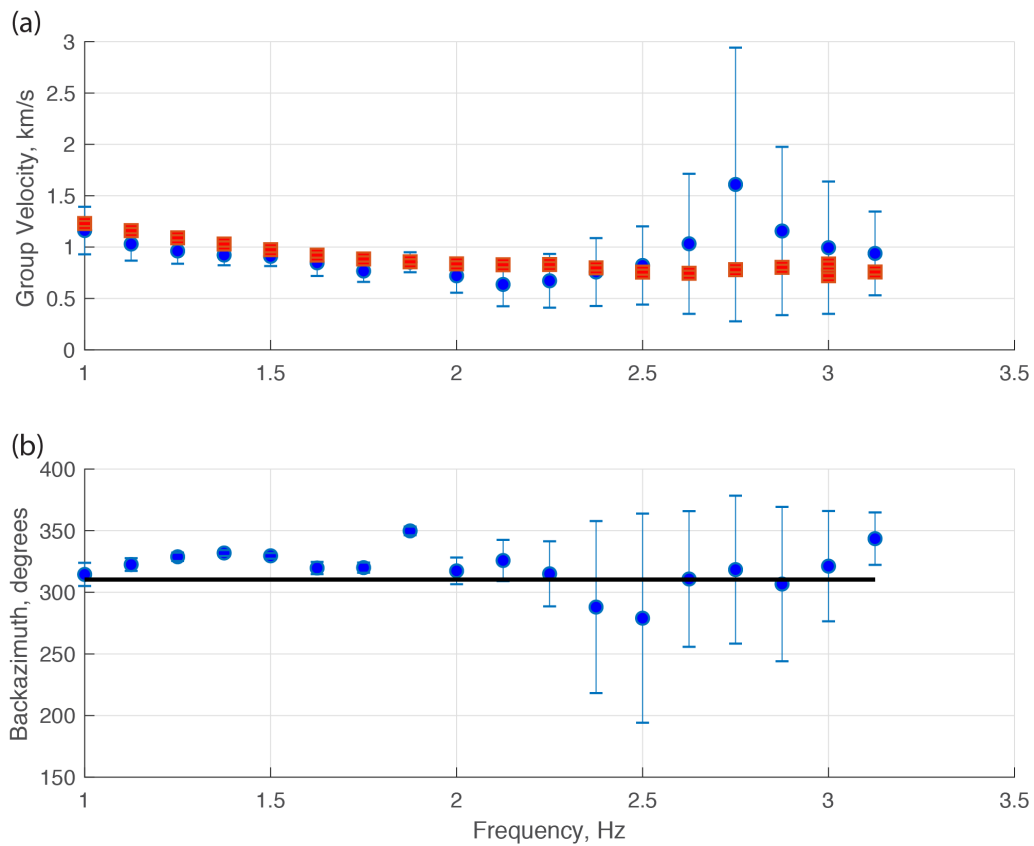


Figure 11 – (a) compares the group velocity determined by array analysis (filled circles) with the whole path group velocity determined by dividing the great circle distance by the group arrival time at station 3016 (filled squares). There seems to be no significant difference in group velocities determine by two independent means. (b) shows the backazimuth determined from the array group velocity analysis as a function of frequency. Multipathing causes the larger errors at frequencies greater than 2.5 Hz.

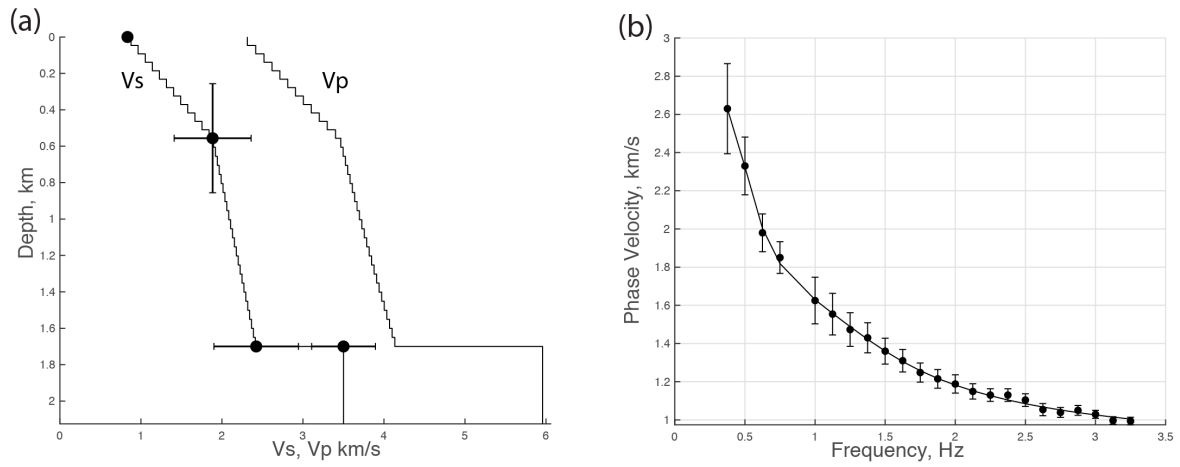


Figure 12 – (a) Velocity model determined from formal inversion of the phase velocity data. (b) Phase velocity data, data errors, and fit (line).

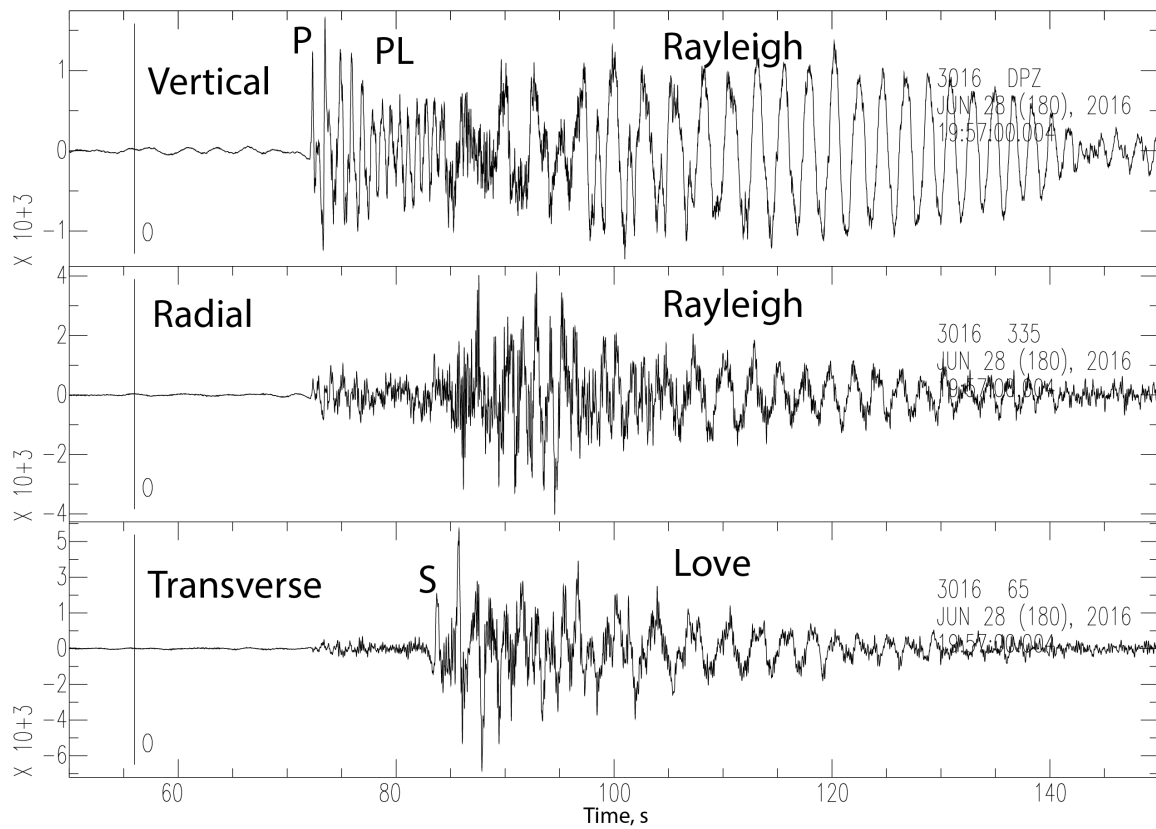


Figure 13 – Waveforms recorded at station 3016 for the M3.6 6/28/2016 Langston, Oklahoma, earthquake. Vertical, radial, and transverse component waveforms are shown. The data have been corrected for instrument response. P, PL, Rayleigh, and Love waves are annotated.

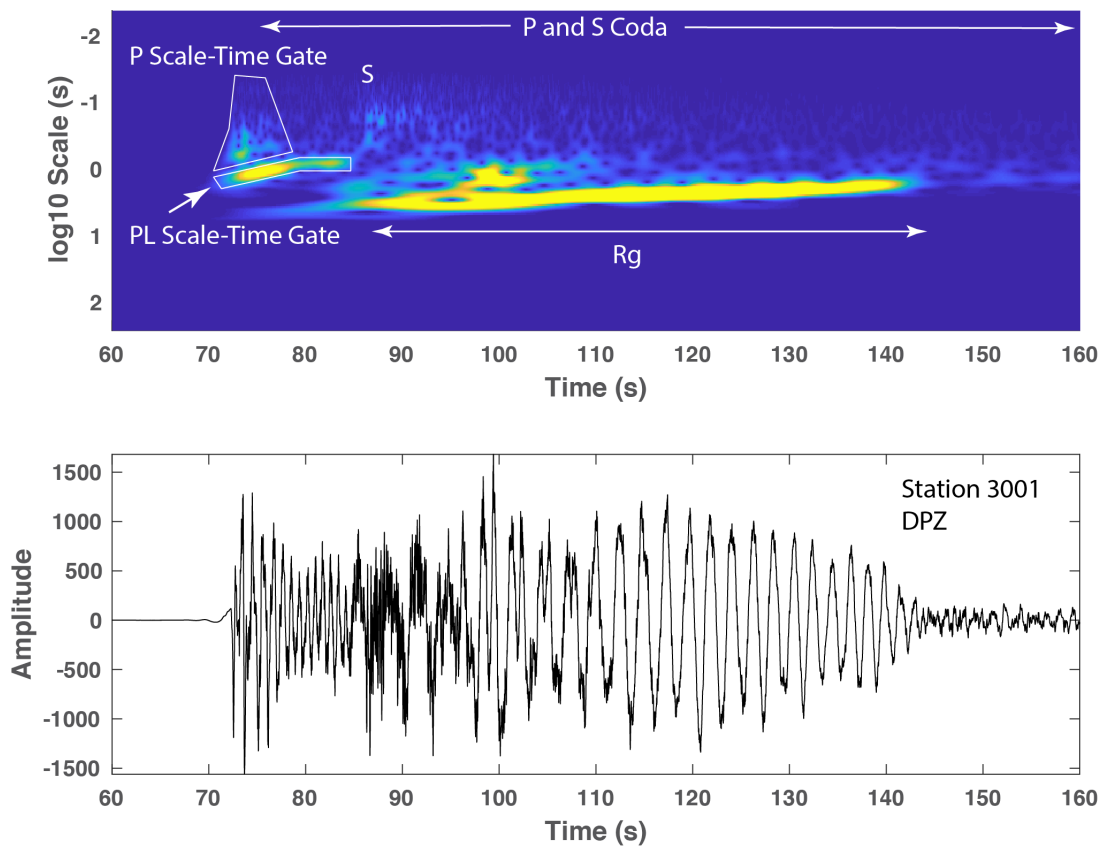


Figure 14 – Scale-time gates chosen for the vertical component of the M3.6 earthquake. The top panel shows the scalogram for the seismogram shown below. Time gate polygons were chosen for the low scale portion of the P wave and harmonic portion of the PL phase. S, Rg, and Coda phases are also annotated.

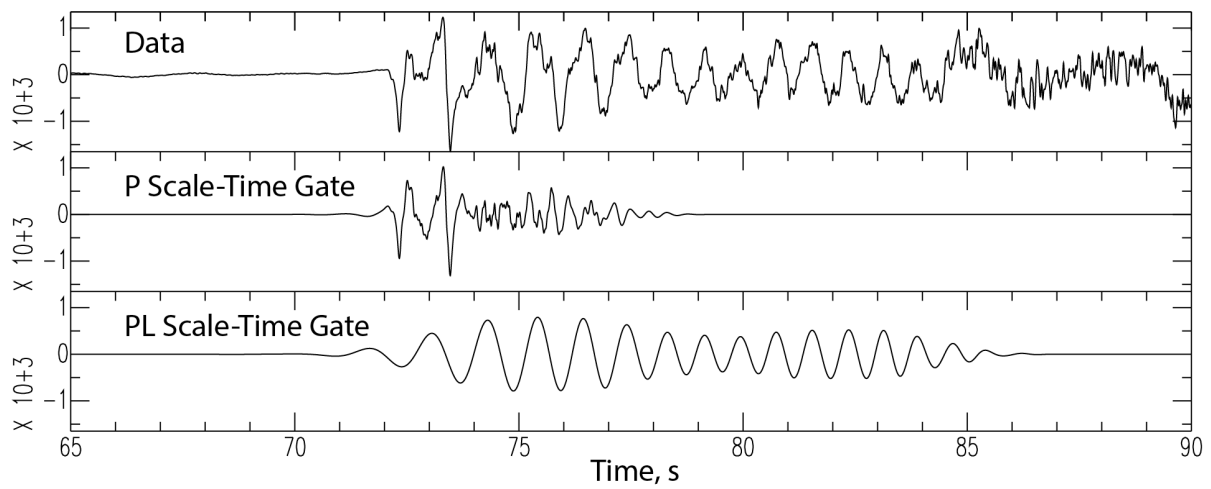


Figure 15 – Results from scale-time gating the vertical component of station 3016 using the P and PL wave gates shown in Figure 16. The original data is shown in the top panel and the gated waveforms shown below.

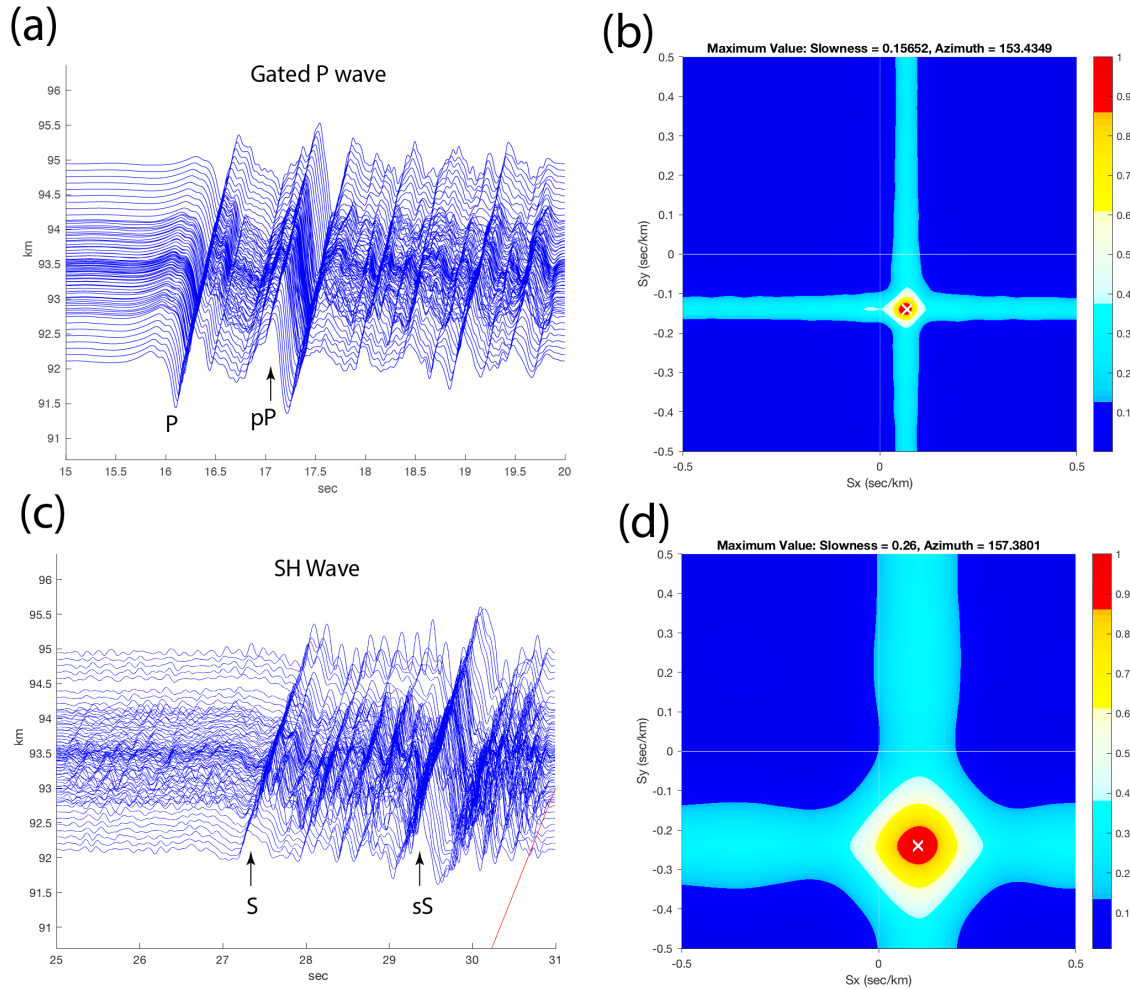


Figure 16 – (a) shows the gated P wave at the 81 stations of the cross array. The broadband f-k beam for 5 to 20Hz is shown in (b) and indicates that the two major phases, denoted by P and pP, have identical slownesses. (c) shows the instrument-corrected SH waves at the cross array with (c) the 1 to 10Hz broadband f-k response. S and sS phases are shown on the seismograms.

Appendix A

This appendix outlines the solution for steering an array to the optimum beam towards the backazimuth to the source using group arrival times of fundamental mode Rayleigh waves.

Assume a Cartesian coordinate system with x being Easting and y being Northing. The group arrival time, t_i , at the i th array station located at (x_i, y_i) is given by

$$t_i = \frac{-\vec{R}_i \cdot \vec{B}}{v} + t_0 \quad (\text{A1})$$

where v is the group velocity and t_0 a reference time. \vec{R}_i is the vector to the i th station given by

$$\vec{R}_i = x_i \hat{e}_1 + y_i \hat{e}_2 \quad (\text{A2})$$

and \vec{B} is the negative of the wave direction vector given by

$$\vec{B} = \sin \theta \hat{e}_1 + \cos \theta \hat{e}_2 \quad (\text{A3})$$

with θ being the backazimuth. The x and y group slownesses are defined by

$$\begin{aligned} \gamma_x &= \frac{\sin \theta}{v} \\ \gamma_y &= \frac{\cos \theta}{v} \end{aligned} \quad . \quad (\text{A4})$$

Given n array stations with group arrival time observations, a linear system of equations can be set up to solve for the x and y group slownesses:

$$\begin{bmatrix} -x_1 & -y_1 \\ -x_2 & -y_2 \\ \vdots & \vdots \\ -x_n & -y_n \end{bmatrix} \begin{bmatrix} \gamma_x \\ \gamma_y \end{bmatrix} = \begin{bmatrix} t_1 - t_0 \\ t_2 - t_0 \\ \vdots \\ t_n - t_0 \end{bmatrix} \quad . \quad (\text{A5})$$

This is of the form of

$$\mathbf{Gm} = \mathbf{d} \quad (\text{A6})$$

893 with the least squares solution

894
$$\mathbf{m} = (\mathbf{G}^T \mathbf{G})^{-1} \mathbf{G}^T \mathbf{d} \quad . \text{ (A7)}$$

895 Define

896

897
$$\mathbf{G}_g^{-1} = (\mathbf{G}^T \mathbf{G})^{-1} \mathbf{G}^T \quad . \text{ (A8)}$$

898 A very conservative estimate of the error is obtained by using the least squares error after

899 inversion

900
$$lse = \|\mathbf{d} - \mathbf{Gm}\|_2 \quad (\text{A7})$$

901 to estimate the model parameter covariance matrix

902

903
$$\mathbf{C} = lse^2 \mathbf{G}_g^{-1} \mathbf{G}_g^{-1^T} \quad (\text{A8})$$

904 where

905

906
$$\begin{aligned} \sigma_{\gamma_x}^2 &= C_{11} \\ \sigma_{\gamma_y}^2 &= C_{22} \end{aligned} \quad . \text{ (A9)}$$

907 The total slowness is given by

908

909
$$\gamma = \left(\gamma_x^2 + \gamma_y^2 \right)^{1/2} \quad (\text{A10})$$

910 and to first order its error

911

912
$$\sigma_\gamma^2 = \left(\gamma_x \sigma_{\gamma_x} + \gamma_y \sigma_{\gamma_y} \right)^2 \quad . \text{ (A11)}$$

913 Backazimuth is given by

914

915
$$\theta = \tan^{-1} \frac{\gamma_x}{\gamma_y} \quad (\text{A12})$$

916 and its error, also to first order, by

917

$$\sigma_{\theta} = \tan^{-1} \left(\frac{\gamma_y \sigma_{\gamma_x} + \gamma_x \sigma_{\gamma_y}}{\gamma_y^2} \right) . \quad (\text{A13})$$

Appendix B

A shear wave velocity model is parameterized by specifying velocity nodes as a function of depth with a linear velocity gradient in between nodes, except at layer boundaries. An example is shown in Figure 12. Shear wave velocity and depth may be the object of the inversion but either parameter may be constrained depending on available data. For example, in Figure 12, the depths of the two nodes at 1.7km are constrained from an acoustic well log taken near the explosion shot point and array (Figure 1b). Because Rayleigh wave phase velocity is relatively insensitive to P wave velocity and density, these parameters are determined from the shear wave velocity. P wave velocity is derived from equation (9) of Brocher (2005) and density from the Nafe-Drake relation, equation (1) of Brocher (2005).

The inversion problem is set up using the “jumping” inversion method of Constable et al. (1987). Phase velocity, c_j , for frequency, f_j , may be a function of v_{si} and h_i , the depth of the node. The problem is linearized the usual way by expanding phase velocity in a Taylor’s series and truncating it at the first term:

$$c_j(\vec{m}) = c_j(\vec{m}_0) + \left. \frac{\partial c}{\partial v_s} \right|_{\vec{m}_0} (v_{s_i} - v_{s_i}^0) + \left. \frac{\partial c}{\partial h} \right|_{\vec{m}_0} (h_i - h_i^0) . \quad (\text{B1})$$

where \vec{m}_0 is the starting model vector. Equation (B1) is manipulated to

$$\left. \frac{\partial c}{\partial v_s} \right|_{\vec{m}_0} (v_{s_i} - v_{s_i}^0) + \left. \frac{\partial c}{\partial h} \right|_{\vec{m}_0} (h_i - h_i^0) = c_j(\vec{m}) - c_j(\vec{m}_0) \quad (\text{B2})$$

to give the matrix relation

941 $\mathbf{G}\Delta\mathbf{m} = \Delta\mathbf{d}. \quad (\text{B3})$

942 The partial derivatives in equation (B1) were calculated using the central finite difference; two
 943 velocity models were calculated for each derivative.

944 The predicted data from the starting model are added to both sides of (B3) to give a linear
 945 problem in the model parameters directly rather than the model parameter changes:

946
$$\begin{aligned} \mathbf{G}\Delta\mathbf{m} + \mathbf{G}\mathbf{m}_0 &= \Delta\mathbf{d} + \mathbf{G}\mathbf{m}_0 \\ \mathbf{G}(\Delta\mathbf{m} + \mathbf{m}_0) &= \mathbf{d} \\ \mathbf{G}\mathbf{m} &= \mathbf{d} \end{aligned} \quad . \quad (\text{B4})$$

947 This problem is iteratively solved using singular value decomposition (e.g., Aster et al., 2005)
 948 where

949
$$\mathbf{G} = \mathbf{U}\mathbf{\Lambda}\mathbf{V}^T \quad (\text{B5})$$

950 and

951
$$\mathbf{G}_g^{-1} = \mathbf{V}\mathbf{\Lambda}^{-1}\mathbf{U}^T \quad . \quad (\text{B6})$$

952 The problem is overdetermined so errors in the parameters are estimated by finding the
 953 covariance matrix of the parameters through

954
$$\mathbf{E}_m = \mathbf{G}_g^{-1}\mathbf{E}_d\left(\mathbf{G}_g^{-1}\right)^T \quad (\text{B7})$$

955 where

956
$$\mathbf{E}_d = \begin{bmatrix} \sigma_1^2 & 0 & 0 & 0 \\ 0 & \sigma_2^2 & 0 & 0 \\ 0 & 0 & \ddots & 0 \\ 0 & 0 & 0 & \sigma_n^2 \end{bmatrix} \quad (\text{B8})$$

958 is the data covariance matrix containing the estimated variances of each measurement of phase
 959 velocity.

960 In application to finding the velocity model of Figure 12, convergence occurred within 4
961 iterations with the largest changes occurring in the first iteration. The error bars in Figure 12 are
962 the standard deviations determined from the diagonal elements of the model covariance matrix
963 and only give an approximate indication of the errors involved. The model covariance matrix
964 has significant off-diagonal terms indicating large trade-off between some parameters such as
965 node depth and velocity.

966 A MatLab code was written to compute phase velocity for plane layered Earth structure using
967 the classical theory presented by Harkrider (1964). Layered models were constructed using the
968 node velocity and positions with thin layers approximating the linear shear wave velocity
969 gradients between nodes. P wave velocity and density were derived from each shear wave value
970 using Brocher's equations mentioned above.

971

972

973